J. Mech. Phys. Solids 153 (2021) 104468

Contents lists available at ScienceDirect

Journal of the Mechanics and Physics of Solids

journal homepage: www.elsevier.com/locate/jmps

An analysis of Lode effects in ductile failure

M.E. Torki [a], S.M. Keralavarma [b], A.A. Benzerga [c,*]

[a] Department of Engineering, University of Cambridge, Trumpington St., Cambridge CB2 1PZ, UK
[b] Department of Aerospace Engineering, Indian Institute of Technology Madras, Chennai 600036, India
[c] Department of Aerospace Engineering, Texas A&M University, College Station, TX 77843, USA

ARTICLE INFO

Keywords:
Fracture mechanisms
Voids and inclusions
Constitutive behavior
Low stress triaxiality
Strain localization
Inhomogeneous yielding

ABSTRACT

An isotropic multi-surface model of porous material plasticity is derived and employed to investigate the effects of the third stress invariant in ductile failure. The constitutive relation accounts for both *homogeneous* and *inhomogeneous* yielding of a material containing a *random* distribution of voids. Individual voids are modeled as spheroidal but the aggregate has no net texture. Ensemble averaging is invoked to operate a scale transition from the inherently anisotropic meso-scale process of single-void growth and coalescence to some macroscopic volume that contains many voids. Correspondingly, expressions for effective yield and associated evolution equations are derived from first principles, under the constraint of *persistent isotropy*. It is found that the well-known vertex on the hydrostatic axis either disappears for sufficiently flat voids or develops into a lower-order singularity for elongated ones. When failure is viewed as the onset of an instability, it invariably occurs after the transition to inhomogeneous yielding with the delay between the two depending strongly upon the Lode parameter. The strain to failure is found to be weakly dependent on the Lode parameter for shear-dominated loadings, but strongly dependent on it near states of so-called generalized tension or compression. Experimentally determined fracture loci for near plane stress states are discussed in light of the new findings.

1. Introduction

Much research has been carried out on low stress-triaxiality ductile failure since the turn of the millennium (Pineau et al., 2016). The central question is the extent to which ductility limits depend on the third stress invariant J_3. Torsion experiments carried out in the 1980s indicate that ductility is generally greater in (pure) torsion than in (simple) tension for a range of materials (Johnson et al., 1983). In tension, plane strain ductility is smaller than axisymmetric ductility with the difference increasing significantly with yield strength (Clausing, 1970). Details aside, these trends are consistent with an effect of the hydrostatic stress, *e.g.* Rice and Tracey (1969), such that a J_3 effect need not be invoked. A way to investigate this effect is to consider combined tension and shear in flat specimens, *e.g.* Bao and Wierzbicki (2004) and Mohr and Marcadet (2015) or combined tension and torsion of tubular specimens (Barsoum and Faleskog, 2007; Scales et al., 2016). For both, near plane stress states are generated so that J_3 and the first stress invariant, I_1, do not vary independently. Available experiments report conflicting results, with some fracture loci exhibiting a cusp (Bao and Wierzbicki, 2004; Barsoum and Faleskog, 2007) while others showing a monotonically increasing strain to failure with decreasing I_1 or triaxiality; see Scales et al. (2016) and references therein.

Experiments alone do not suffice to draw definite conclusions on the extent of an effect of J_3, or equivalently its nondimensional counterpart known as the Lode parameter. A conceptual difficulty is that large plastic strains accrue at the low triaxiality states of

* Corresponding author.
E-mail address: benzerga@tamu.edu (A.A. Benzerga).

https://doi.org/10.1016/j.jmps.2021.104468
Received 30 January 2021; Received in revised form 13 April 2021; Accepted 23 April 2021
Available online 30 April 2021

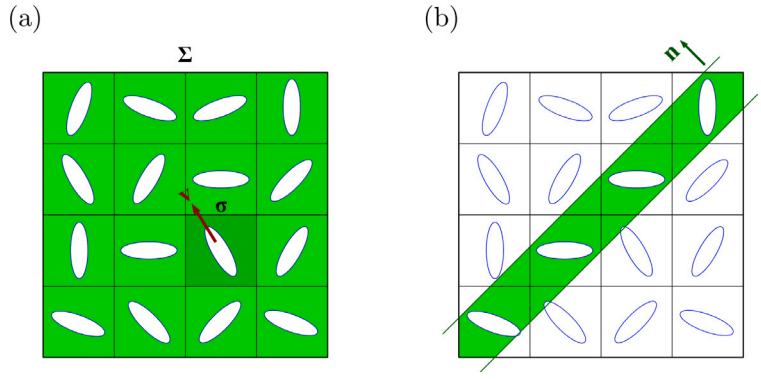

Fig. 1. Schematic distribution of non-spherical voids with random orientations under (a) homogeneous yielding and (b) inhomogeneous yielding determined by band orientation **n**.

interest so that various forms of induced anisotropy manifest, unavoidably (Roth et al., 2018). Neither plasticity nor damage are expected to proceed in an isotropic manner so that the question under investigation is generally ill-posed, experimentally speaking. Notwithstanding this difficulty, one may investigate the issue theoretically under conditions to be specified.

Phenomenological models incorporating a Lode effect have received wide attention, *e.g.* Bai and Wierzbicki (2010) and Mohr and Marcadet (2015). They rely on an *ad hoc* representation of the fracture process with no underlying damage mechanism. On the other hand, Nahshon and Hutchinson (2008) extended the Gurson model (Gurson, 1977; Tvergaard, 1982) of porous material plasticity to explicitly include the effect of J_3 in the evolution equation of the void volume fraction. Unless the latter is reinterpreted as a structureless internal variable, this amendment to the Gurson model violates mass conservation. In addition, what form the J_3-dependent contribution to the growth rate of damage should take remains arbitrary as no conclusive assessment against experiments has been demonstrated; see *e.g.* Dunand and Mohr (2011).

Here, we consider a statistically isotropic distribution of voids in a plastic material. The voids are non-spherical and identical in shape but are randomly oriented so that no net texture remains at the macro-scale, Fig. 1. The instantaneous response of the void aggregate is thus isotropic. Any effects of an evolving texture are neglected such that the property of statistical isotropy is assumed to persist under finite deformations. Only under such an admittedly strong assumption can Lode effects be investigated.

(Rate-independent) yielding is assumed to occur either by diffuse plasticity in the entire matrix, Fig. 1a, or by localized plasticity in one or more bands, Fig. 1b. The former is referred to as homogeneous yielding (HY), the latter inhomogeneous yielding (IY). Micromechanics-based yield criteria for each mechanism have previously been derived by 'homogenization' and limit analysis of a smaller unit cell containing an isolated void, *e.g.* Keralavarma and Benzerga (2010), Torki et al. (2015) and Keralavarma and Chockalingam (2016). Unlike in these prior works, three scales are now relevant. The microscale is that of the matrix, resolving the intervoid spacing. The meso-scale refers to the average response of the single-void cell, which is generally anisotropic. Finally, the macro-scale is that of the void aggregate with statistical isotropy. Scale separation is assumed to hold in the usual sense (Benzerga and Leblond, 2010) although difficulties inevitably arise with inhomogeneous yielding (Morin et al., 2016).

In general, failure may occur due to porosity growth or due to a macroscopic plastic instability. When observed, porosity growth may be enhanced after the onset of inhomogeneous yielding thus leading to a complete loss of load bearing capacity upon coalescence (Koplik and Needleman, 1988; Benzerga, 2002). However, the process is generally anisotropic. In addition, under shear-dominated loading, the onset of inhomogeneous yielding does not necessarily lead to loss of load bearing capacity. Therefore, not only some isotropic model of inhomogeneous yielding is needed, but also the HY–IY transition does not necessarily correspond to failure under general loadings (Torki and Benzerga, 2018). Here, failure is identified with the onset of a macroscopic instability (Rice, 1976) so as to encompass diverse stress states. The instability condition is sought using constitutive relations that account for competing modes of plastic flow within a multi-surface representation of (isotropic) porous material plasticity. To investigate Lode effects, the constitutive relations are integrated under prescribed proportional loading paths until an instability eventually occurs. Readers not familiar with the distinction between strain localization and inhomogeneous yielding, which is a form of *finite* strain concentration, should consult prior work; see *e.g.* Morin et al. (2016).

The paper is organized as follows. In Section 2 macroscopically isotropic yield criteria are developed by ensemble averaging on the basis of available mesoscopically anisotropic criteria. Section 3 lists all relevant constitutive relations, including elasticity, hardening and evolution equations of two state variables related to porosity. A failure criterion is developed in Section 4 on the basis of strain localization in a material obeying the constitutive relations of Section 3. Results are presented in Section 5 laying emphasis on (i) features of effective yield surfaces; (ii) failure loci under plane stress loadings; (iii) failure loci under more general, proportional loadings. The results are discussed in Section 6 in light of current understanding and available experiments.

2. Derivation of yield criteria

2.1. Homogeneous yielding

2.1.1. Meso-scale criterion

Void growth is described using the criterion developed by Keralavarma and Benzerga (2010), which for an isotropic matrix reduces to that of Gologanu et al. (1997). The elementary cell contains a *single* spheroidal void oriented using unit vector $\mathbf{v}$, Fig. 1a. At the meso-scale, the yield function reads

$$\mathcal{F}^{\mathrm{H}}(\boldsymbol{\sigma};\mathbf{v},f,w)=\frac{3}{2}C\frac{\boldsymbol{\sigma}:\mathbb{K}:\boldsymbol{\sigma}}{\bar{\sigma}^2}+2(g+1)(g+f)\cosh\left(\kappa\frac{\boldsymbol{\sigma}:\mathbf{X}}{\bar{\sigma}}\right)-(g+1)^2-(g+f)^2 \tag{1}$$

where $\boldsymbol{\sigma}$ is the cell-averaged stress, f is the void volume fraction, w is the void aspect ratio (greater than unity for prolate voids), and $\bar{\sigma}$ is the matrix yield strength. Also, $\mathbf{X}$ is a second order tensor given by:

$$\mathbf{X}=(1-3\alpha_2)\mathbf{v}\otimes\mathbf{v}+\alpha_2\mathbf{I}, \tag{2}$$

with $\alpha_2(f,w)$ a function of internal variables f and w, and $\mathbf{I}$ the second-order identity tensor. In addition, $\mathbb{K}$ is a fourth order effective anisotropy tensor given by:

$$\mathbb{K}=\mathbb{J}+\eta\,(\mathbf{X}\otimes\mathbf{Q}+\mathbf{Q}\otimes\mathbf{X}) \tag{3}$$

Here, $\mathbb{J}=\mathbb{I}-\frac{1}{3}\mathbf{I}\otimes\mathbf{I}$ denotes the deviatoric projection tensor, $\mathbb{I}$ is the fourth-order identity tensor and the tensor $\mathbf{Q}$ is given by:

$$\mathbf{Q}=\frac{3}{2}\mathbf{v}\otimes\mathbf{v}-\frac{1}{2}\mathbf{I} \tag{4}$$

Finally, C, η, g and κ are, just like α_2, functions of f and w. Their expressions can be found in Keralavarma and Benzerga (2010). For spherical voids ($w=1$), $C=1$, $\eta=0$, $g=0$, $\kappa=3/2$ and $\alpha_2=1/3$.

2.1.2. Macro-scale criterion

Criterion (1) is used to describe yielding at the meso-scale. Accordingly, an admissible (meso-scale) stress satisfies the inequality

$$\frac{3}{2}C\frac{\boldsymbol{\sigma}:\mathbb{K}:\boldsymbol{\sigma}}{\bar{\sigma}^2}\le(g+1)^2+(g+f)^2-2(g+1)(g+f)\cosh\left(\kappa\frac{\boldsymbol{\sigma}:\mathbf{X}}{\bar{\sigma}}\right) \tag{5}$$

All voids in the aggregate of Fig. 1a are assumed to be identical in shape. However, the void orientation $\mathbf{v}$, and therefore tensors $\mathbf{X}$, $\mathbf{Q}$ and $\mathbb{K}$, vary from cell to cell. Averaging over all constituent unit cells of the aggregate leads to an isotropic macroscopic yield criterion. Assuming equal volumes among all voids, the volume average can be replaced with an ensemble average $\langle\cdot\rangle$ over all possible void orientations, yielding

$$\left\langle\frac{3}{2}C\frac{\boldsymbol{\sigma}:\mathbb{K}:\boldsymbol{\sigma}}{\bar{\sigma}^2}\right\rangle\le\left\langle(g+1)^2+(g+f)^2-2(g+1)(g+f)\cosh\left(\kappa\frac{\boldsymbol{\sigma}:\mathbf{X}}{\bar{\sigma}}\right)\right\rangle \tag{6}$$

Scalar functions C, η, g, κ and α_2 are independent of $\mathbf{v}$, since they only depend on f and w. Also, the concave nature of $\cosh x$ yields $\langle\cosh x\rangle\ge\cosh\langle x\rangle$, hence the above inequality further simplifies to:

$$\frac{3}{2}C\frac{\langle\boldsymbol{\sigma}:\mathbb{K}:\boldsymbol{\sigma}\rangle}{\bar{\sigma}^2}\le(g+1)^2+(g+f)^2-2(g+1)(g+f)\cosh\left(\kappa\frac{\langle\boldsymbol{\sigma}:\mathbf{X}\rangle}{\bar{\sigma}}\right) \tag{7}$$

The remaining averages can only be determined in an approximate sense, since the variation of the mesoscopic stress tensor $\boldsymbol{\sigma}$ from cell to cell, due to the change in local void orientation, cannot be estimated analytically. Instead, we resort to the same Reuss-type approximation employed by Gologanu et al. (1993) by neglecting the above dependence of $\boldsymbol{\sigma}$ on $\mathbf{v}$ and equate the meso- and macro-scale stress tensors; *i.e.* $\boldsymbol{\sigma}=\boldsymbol{\Sigma}$. With this admittedly crude approximation, the previous inequality simplifies to

$$\frac{3}{2}C\frac{\boldsymbol{\Sigma}:\langle\mathbb{K}\rangle:\boldsymbol{\Sigma}}{\bar{\sigma}^2}\le(g+1)^2+(g+f)^2-2(g+1)(g+f)\cosh\left(\kappa\frac{\boldsymbol{\Sigma}:\langle\mathbf{X}\rangle}{\bar{\sigma}}\right) \tag{8}$$

It is straightforward to show that

$$\langle\mathbf{X}\rangle=\frac{1}{3}\mathbf{I}, \tag{9}$$

based on definition (2) since $\langle\mathbf{v}\otimes\mathbf{v}\rangle=\frac{1}{3}\mathbf{I}$. Hence, the term $\boldsymbol{\Sigma}:\langle\mathbf{X}\rangle$ reduces to the mean normal stress $\Sigma_{\mathrm{m}}=\frac{1}{3}\Sigma_{kk}$. Also, from (4) we have $\langle\mathbf{Q}\rangle=\mathbf{0}$.

Next, consider the orientation average of tensor $\mathbb{K}$ in Eq. (3) as

$$\langle\mathbb{K}\rangle=\mathbb{J}+\eta\langle\mathbf{X}\otimes\mathbf{Q}+\mathbf{Q}\otimes\mathbf{X}\rangle \tag{10}$$

Using the above results for $\langle\mathbf{X}\rangle$ and $\langle\mathbf{Q}\rangle$ the second term in the above equation evaluates to

$$\langle\mathbf{X}\otimes\mathbf{Q}+\mathbf{Q}\otimes\mathbf{X}\rangle=(1-3\alpha_2)\left[3\langle\mathbf{V}\otimes\mathbf{V}\rangle-\frac{1}{3}\mathbf{I}\otimes\mathbf{I}\right] \tag{11}$$

with $\mathbf{V} = \mathbf{v} \otimes \mathbf{v}$ and thus

$$\langle \mathbf{V} \otimes \mathbf{V} \rangle = \frac{2}{15}\mathbb{J} + \frac{1}{9}\mathbf{I} \otimes \mathbf{I} \tag{12}$$

Substituting (11) and (12) into (10) leads to:

$$\langle \mathbb{K} \rangle = \left[1 + \frac{2}{5}\eta(1 - 3\alpha_2)\right]\mathbb{J} \tag{13}$$

Using this result in inequality (8) we obtain, after rearranging

$$\bar{\mathcal{F}}^{\mathrm{H}}(\boldsymbol{\Sigma}; f, w) = \bar{C}\frac{\Sigma_{\mathrm{eq}}^2}{\bar{\sigma}^2} + 2(g+1)(g+f)\cosh\left(\kappa\frac{\Sigma_{\mathrm{m}}}{\bar{\sigma}}\right) - (g+1)^2 - (g+f)^2 \leq 0 \tag{14}$$

where $\Sigma_{\mathrm{eq}} = \sqrt{\frac{3}{2}\boldsymbol{\Sigma}' : \boldsymbol{\Sigma}'}$ is the macroscopic von Mises equivalent stress and

$$\bar{C} = C\left[1 + \frac{2}{5}\eta(1 - 3\alpha_2)\right] \tag{15}$$

Eq. (14) represents the macroscopic isotropic criterion for homogeneous yielding accounting for a random orientation of spheroidal voids. In the special case of spherical voids, $\eta = 0$, $C = 1, \kappa = \frac{3}{2}$ and $g = 0$, so that Gurson's yield criterion is recovered.

2.2. Inhomogeneous yielding

2.2.1. Meso-scale criterion

Inhomogeneous yielding refers to plastic deformation localizing into the intervoid ligament, with the rest of the cell unloading elastically. In a cylindrical cell containing a single coaxial void, the orientation $\mathbf{n}$ of the plastic band is thus set by that of the ligament. Criteria for this (mesoscopic) mode of yielding have been developed by Benzerga and Leblond (2014) for tension and by Torki et al. (2015) and Keralavarma and Chockalingam (2016) for combined tension and shear. The effective yield criterion derived by Torki et al. (2015) writes:

$$\mathcal{F}^{\mathrm{I}}(\boldsymbol{\sigma}; f_{\mathrm{b}}, w, \mathbf{n}) = \frac{\langle\langle |\sigma_{\mathrm{n}}| - S \rangle\rangle^2}{\mathcal{V}^2} + \frac{\tau_{\mathrm{n}}^2}{\mathcal{T}^2} - 1 = 0 \tag{16}$$

where $\boldsymbol{\sigma}$ refers to the mesoscale stress with band-resolved normal and shear tractions σ_{n} and τ_{n}, respectively, $\langle\langle\cdot\rangle\rangle$ stand for Macaulay brackets ($\langle\langle x \rangle\rangle = x$ for $x > 0$, zero otherwise) and $\mathcal{S}(f_{\mathrm{b}}, w)$, $\mathcal{V}(f_{\mathrm{b}})$ and $\mathcal{T}(f_{\mathrm{b}})$ are functions given by:

$$\begin{aligned} &\mathcal{V}/\bar{\tau} = 2 - \sqrt{1 + 3f_{\mathrm{b}}^2} + \ln\frac{1 + \sqrt{1 + 3f_{\mathrm{b}}^2}}{3f_{\mathrm{b}}} \\ &\mathcal{S}/\bar{\tau} = \frac{f_{\mathrm{b}}^{3/2} - 3\sqrt{f_{\mathrm{b}}} + 2}{3\sqrt{f_{\mathrm{b}}}w}; \qquad \mathcal{T}/\bar{\tau} = (1 - f_{\mathrm{b}}) \end{aligned} \tag{17}$$

with $\bar{\tau} = \bar{\sigma}/\sqrt{3}$ the matrix shear strength, f_{b} the *band porosity*, Fig. 1b, and w the void aspect ratio. Criterion (16) provides a tight upper bound to the exact yield surface under inhomogeneous yielding for a wide range of internal variables f_{b} and w (Torki et al., 2015, 2017). Heuristic factors t, b, l may be introduced, respectively multiplying the terms $\mathcal{S}$, $\mathcal{V}$, $(1 - f_{\mathrm{b}})$ in (16). As argued by Torki et al. (2017) this modification is warranted for penny-shaped cracks ($w \to 0$) and, to a lesser extent, for very long voids ($w \gg 1$); see Appendix B.

An alternative yield criterion was developed by Keralavarma and Chockalingam (2016) who used a continuous trial velocity field, first introduced by Morin et al. (2015), in the limit analysis of the single-void cell instead of the discontinuous field used by Torki et al. (2015). For a von Mises matrix, their criterion reads

$$\mathcal{F}^{\mathrm{I}} = 3\frac{\tau_{\mathrm{n}}^2}{\bar{\sigma}^2} + 2f_{\mathrm{b}}\cosh\left(\beta\frac{\sigma_{\mathrm{n}}}{\bar{\sigma}}\right) - \left(1 + f_{\mathrm{b}}^2\right) = 0 \tag{18}$$

with

$$\begin{aligned} &\beta(f_{\mathrm{b}}, w) = \sqrt{\frac{5}{6}}\ln\left(\frac{1}{f_{\mathrm{b}}}\right)\left[\sqrt{b^2+1} - \sqrt{b^2 + f_{\mathrm{b}}^2} + b\ln\left(\frac{b + \sqrt{b^2 + f_{\mathrm{b}}^2}}{f_b\left(b + \sqrt{b^2+1}\right)}\right)\right]^{-1} \\ &b = \sqrt{\frac{1}{3} + \frac{5\alpha}{24\mathcal{W}^2}} \quad , \quad \alpha = \frac{1}{12}\left[1 + f_{\mathrm{b}} - 5(f_{\mathrm{b}})^2 + 3(f_{\mathrm{b}})^3\right] \end{aligned} \tag{19}$$

where $\mathcal{W}$ is a function of f_{b} and w, calibrated against numerical results and given by

$$\mathcal{W} = \begin{cases} \dfrac{f_{\mathrm{b}}w^2}{4\mathcal{W}_0} + \mathcal{W}_0 & \text{for } \sqrt{f_{\mathrm{b}}}w < 2\mathcal{W}_0 \\ \sqrt{f_{\mathrm{b}}}w & \text{for } \sqrt{f_{\mathrm{b}}}w \geq 2\mathcal{W}_0 \end{cases} \tag{20}$$

with $\mathcal{W}_0$ an adjustable parameter close to 0.1. Criterion (18) is not a rigorous upper bound. However, it provides robust estimates and, most importantly, is smooth with no singular parts (flat parts on the yield locus). This is important for macroscopic strain localization; see Section 4.

2.2.2. Macro-scale criterion

Criteria (16) and (18) are both transversely isotropic since they depend on the orientation of the plastic band defined by $\mathbf{n}$. A more general criterion for arbitrary void and band orientations is lacking. A way to obtain a macroscopically isotropic criterion of inhomogeneous yielding is to consider the average response over random void orientations assuming that yielding occurs in a band that minimizes the effective yield stress. In this view, the operation performed over all band orientations is an extremization, which is different from ensemble averaging. Also, heuristics is introduced to relax the void–cell coaxiality inherent to the mesoscale criteria (16) and (18). This is done by introducing a surrogate void aspect ratio, $\bar{w}$. Torki and Benzerga (2018) used a similar approach in their analysis of failure in shear. Such heuristics consists of making the general case amenable to void–cell coaxiality. With technical details deferred to Appendix A, the surrogate parameters f_b and $\bar{w}$ are obtained from the actual parameters f and w using the relations:

$$f_\mathrm{b}^{\frac{3}{2}}\bar{w} = f \tag{21}$$

$$\bar{w} = \begin{cases} w\left[\frac{2}{\pi}K\left(1-\frac{1}{w^2}\right)\right]^{-3/2} & (w \geq 1) \\ \frac{1}{\sqrt{w}}\left[\frac{2}{\pi}K\left(1-w^2\right)\right]^{-3/2} & (w < 1) \end{cases} \tag{22}$$

where K denotes the complete elliptic integral of the first kind.

In a statistically isotropic dispersion of voids, the orientation of the plastic band $\mathbf{n}$ is determined chiefly by the state of stress (Keralavarma, 2017). The effective isotropic criterion for inhomogeneous yield determines the region in stress space that lies at the intersection of the yield domains corresponding to all possible orientations of the plastic band. The corresponding (isotropic) yield function is then obtained by maximizing individual (anisotropic) yield functions over all possible orientations:

$$\bar{\mathcal{F}}^{\mathrm{I}}(\boldsymbol{\Sigma}; f_\mathrm{b}, \bar{w}) = \max_{\mathbf{n}^*}\{\mathcal{F}^{\mathrm{I}}(\boldsymbol{\sigma}; f, w, \mathbf{n}^*)\} \tag{23}$$

where $\mathbf{n}^*$ is a unit vector and $\mathcal{F}^{\mathrm{I}}$ is given by either (16) or (18). The bar over the yield function on the left hand-side term indicates sweeping over band orientations (by maximization) as well as averaging over void orientations via the surrogate microstructure; hence the argument $\bar{w}$. Using again a Reuss approximation, the maximization in Eq. (23), at fixed $\boldsymbol{\Sigma}$, leads to the following optimality condition (Keralavarma, 2017)

$$\frac{\partial \mathcal{F}^{\mathrm{I}}}{\partial \mathbf{n}}^* = (\boldsymbol{\Sigma}^2 - \tilde{\Sigma}\boldsymbol{\Sigma})\mathbf{n}^* = 2\lambda\mathbf{n}^* \tag{24}$$

where λ is a Lagrange multiplier and $\tilde{\Sigma}(\boldsymbol{\Sigma}, \mathbf{n}^*)$ is a criterion-sensitive scalar-valued function, to be specified. Thus, the sought orientation $\mathbf{n}$ must be an eigenvector of $\boldsymbol{\Sigma}^2 - \tilde{\Sigma}\boldsymbol{\Sigma}$. Let $\Sigma_1 \geq \Sigma_2 \geq \Sigma_3$ be the principal stresses corresponding to principal directions $\mathbf{e}_1, \mathbf{e}_2, \mathbf{e}_3$. Two cases emerge: (i) either $\mathbf{n}$ is an eigenvector of $\boldsymbol{\Sigma}$; or (ii) $\mathbf{n}$ is a linear combination of two eigenvectors. This only occurs if an eigenvalue of $\boldsymbol{\Sigma}$ is degenerate, say $\Sigma_1 = \Sigma_2$ (trivial case), or if an eigenvalue of $\boldsymbol{\Sigma}^2 - \tilde{\Sigma}\boldsymbol{\Sigma}$ is degenerate while $\Sigma_1 \neq \Sigma_2$; this holds when

$$\tilde{\Sigma}(\boldsymbol{\Sigma}, \mathbf{n}) = \Sigma_1 + \Sigma_2 \tag{25}$$

Case (i) corresponds to coalescence by internal necking of ligaments connecting an array of voids transverse to a principal stress direction. Case (ii) corresponds to inhomogeneous yielding (not necessarily coalescence) under combined tension and shear.

Using criterion (16) as a basis at the meso-scale, internal necking transverse to any of the principal directions is described by yield functions of the form

$$\mathcal{F}^{\mathrm{In}}(\Sigma_i) = \frac{\langle\langle|\Sigma_i| - S\rangle\rangle^2}{\mathcal{Y}^2} - 1, \qquad i = 1 \ldots 3 \tag{26}$$

since the shear traction, which appears in (16), vanishes on a principal plane.

Yielding by combined tension and shear is possible when (25) is satisfied. With $\tilde{\Sigma}$ in (24) given by

$$\tilde{\Sigma}(\boldsymbol{\Sigma}, \mathbf{n}^*) = 2\Sigma_\mathrm{n} - 2\eta\,\mathrm{sgn}\left(\Sigma_\mathrm{n}\right)\langle\langle|\Sigma_\mathrm{n}| - S\rangle\rangle, \qquad \eta \equiv \frac{\mathcal{T}^2}{\mathcal{Y}^2} \tag{27}$$

and $\Sigma_\mathrm{n} = \mathbf{n}^* \cdot \boldsymbol{\Sigma}\mathbf{n}^*$ the traction normal to the band, Eq. (25) reduces, for the optimal band, to

$$\Sigma_\mathrm{n} = \begin{cases} \dfrac{|\Sigma_1 + \Sigma_2| - 2\eta S}{2(1-\eta)}\mathrm{sgn}\left(\Sigma_1 + \Sigma_2\right) & \text{if } |\Sigma_1 + \Sigma_2| > 2S \\ \dfrac{\Sigma_1 + \Sigma_2}{2} & \text{if } |\Sigma_1 + \Sigma_2| \leq 2S \end{cases} \tag{28}$$

subject to the constraint $\Sigma_2 < \Sigma_n < \Sigma_1$ since, in this case, $\mathbf{n}$ lies in the $\mathbf{e}_1$–$\mathbf{e}_2$ principal plane. In obtaining $(28)_1$ one notes that Σ_n has the sign of $\Sigma_1 + \Sigma_2$ since $S \geq 0$ and η defined in $(27)_2$ is smaller than unity for any value of f_b. Accounting for the above constraint on Σ_n is equivalent to

$$D(\Sigma_1, \Sigma_2) \equiv \frac{\eta}{(1-\eta)} \frac{|\Sigma_1 + \Sigma_2| - 2S}{|\Sigma_1 - \Sigma_2|} < 1 \tag{29}$$

Only when this condition is met does yielding under combined tension and shear become possible. The corresponding shear traction ($\Sigma_{sh} = \tau_n$) is obtained from the Mohr identity:

$$\left[\Sigma_n - \left(\frac{\Sigma_1 + \Sigma_2}{2}\right)\right]^2 + \Sigma_{sh}^2 = \left(\frac{\Sigma_1 - \Sigma_2}{2}\right)^2 \tag{30}$$

and the solution is completed by specifying the orientation of the normal to the plastic band, solution of (23). If φ denotes the (signed) band normal angle, measured from $\mathbf{e}_1$, then:

$$\varphi = \frac{1}{2}\sin^{-1}\left(\frac{2\Sigma_{sh}}{\Sigma_1 - \Sigma_2}\right) = \frac{1}{2}\sin^{-1}\left(\frac{2\sqrt{(\Sigma_1 - \Sigma_n)(\Sigma_n - \Sigma_2)}}{\Sigma_1 - \Sigma_2}\right) \tag{31}$$

where use has been made of (30) to obtain the latter expression for convenience. Thus, $\varphi = \pi/4$ if $|\Sigma_1 + \Sigma_2| \leq 2S$. Otherwise, an alternative expression for the normal is:

$$\mathbf{n} = \sqrt{\frac{1+D}{2}}\mathbf{e}_1 + \sqrt{\frac{1-D}{2}}\mathbf{e}_2 \tag{32}$$

where D is given by (29). Eq. (32) gives $\mathbf{n}$ in terms of principal stresses and porosity attributes.

By virtue of (23), the pair $\{\Sigma_n, \Sigma_{sh}\}$ satisfies a yield condition of type (16) with due account of the surrogate microstructure concept. Substituting expressions (28) and (30) for Σ_n and Σ_{sh} in Eq. (16) and simplifying leads to the following criterion:

$$F^{I^{sh}}(\Sigma_1, \Sigma_2) = \frac{\langle\langle |\Sigma_1 + \Sigma_2| - 2S \rangle\rangle^2}{4(\mathcal{V}^2 - \mathcal{T}^2)} + \frac{(\Sigma_1 - \Sigma_2)^2}{4\mathcal{T}^2} - 1, \qquad \text{if } D(\Sigma_1, \Sigma_2) < 1 \tag{33}$$

where S, $\mathcal{V}$ and $\mathcal{T}$ must now be viewed as functions of f_b and $\bar{w}$. Similarly, two concurrent criteria corresponding to the band normal $\mathbf{n}$ lying on the remaining two principal planes can be obtained by cyclic permutation of the indices $(1, 2, 3)$ in Eq. (33).

Finally, the macroscopic (or effective) locus of inhomogeneous yielding for a random dispersion of voids is determined from (23) as:

$$\bar{F}^I(\boldsymbol{\Sigma}; f_b, \bar{w}) = \max_{i \neq j}\left\{F^{I^n}(\Sigma_i), F^{I^{sh}}(\Sigma_i, \Sigma_j)\right\} \qquad i = 1, 2, 3 \tag{34}$$

that is, accounting for the three criteria (26) for internal necking and the three criteria (33) for combined tension and shear yielding.

A similar procedure is followed if criterion (18) is used as basis at the mesoscale. This is documented in Appendix C.

Remark. To obtain the HY model, two successive homogenizations were employed to get from the micro-scale to the meso-scale, then from the latter to the macro-scale. Conceptually, this could also be done for the inhomogeneous yield (IY) model. An attempt in this direction is reported in Appendix B. From the strict viewpoint of homogenization theory, scale separation may be questionable for IY, especially under tension-dominated loading where IY is synonymous with void coalescence. When coalescence occurs, the overall mechanical fields may vary significantly over small distances. The larger the elementary volume considered the closer one gets to the limits of applicability of any homogenization procedure. Another way to approach this issue, is to invoke the argument of Morin et al. (2016) that coalescence usually involves a few voids. The issue then becomes that of determining the orientation of the coalescence band. If the material is isotropic then each void may be viewed as located at the center of a sphere, locus of the centers of nearest neighbors. Then, the size of the 'elementary volume' need not be much larger than that for a periodic distribution, the only difference being the number of nearest neighbors. The latter is finite (and small) for periodic distributions, but infinite for a random one, and the coalescence orientation solely rests on the macroscopic stress state.

3. Constitutive relations

For analysis, the macroscopic yield criteria developed in the previous section are supplemented with constitutive prescriptions for elasticity, a flow rule, strain hardening, and evolution of the internal variables. Assuming small elastic strains, the total rate of deformation $\mathbf{D}$ is additively decomposed into an elastic part, $\mathbf{D}^e$, and a plastic part, $\mathbf{D}^p$, with

$$\mathbf{D} = \mathbf{D}^e + \mathbf{D}^p, \qquad \mathbf{D}^e = \mathbb{C}^{-1} :\overset{\nabla}{\boldsymbol{\Sigma}}, \qquad \mathbf{D}^p = \dot{\Lambda}\mathbf{N} \tag{35}$$

where $\mathbb{C}$ is the fourth-order (isotropic) elastic stiffness tensor, $\overset{\nabla}{\boldsymbol{\Sigma}}$ denotes the Jaumann stress rate, and tensor $\mathbf{N}$ sets the direction of plastic flow, $\dot{\Lambda}$ being the plastic multiplier.

3.1. Multisurface associative criterion

The competition between homogeneous yielding, criterion (14), and inhomogeneous yielding, criterion (34), is accounted for within a multi-surface approach. Thus, the effective yield criterion for a statistically isotropic dispersion of voids is expressed as

$$\mathcal{F}(\boldsymbol{\Sigma}; f, w) = \max\left\{\bar{\mathcal{F}}^{\mathrm{H}}(\boldsymbol{\Sigma}; f, w), \bar{\mathcal{F}}^{\mathrm{I}}(\boldsymbol{\Sigma}; f_{\mathrm{b}}, \bar{w})\right\} \leq 0 \tag{36}$$

with f_{b} and $\bar{w}$ related to f and w through Eqs. (21) and (22). Inhomogeneous yielding includes both internal necking through (26) and combined tension and shear yielding through (33). In other words, the locus defined by $\bar{\mathcal{F}}^{\mathrm{I}} = 0$ itself results from the intersection of six convex domains; see Eq. (34).

Because of the multiple yielding mechanisms, the effective yield surface defined through (36) has vertices. These are of two types: (i) those inherent to the surface $\bar{\mathcal{F}}^{\mathrm{I}} = 0$; (ii) those related to a transition from homogeneous to inhomogeneous yielding.

An associated flow model is employed whereby the direction of plastic flow is taken to be normal to the yield surface wherever the latter is smooth:

$$\mathbf{N} = \frac{\partial \mathcal{F}}{\partial \boldsymbol{\Sigma}} \tag{37}$$

No special treatment of vertices is advanced here. We simply note that type (i) can be handled as in a Tresca yield model as they are known a priori. Their physical meaning is clear, within a rate-independent description, as they are associated with non-uniqueness of the orientation of the plastic band for inhomogeneous yielding, as will be shown in context below for special loading paths. Vertices of type (ii) are induced by plastic deformation and are strongly history-dependent. They are in fact non-physical, as they result from obtaining HY and IY criteria from different, unrelated theoretical sources; see *e.g.* Morin et al. (2016) and Torki (2019). Here, the transition is treated explicitly.

Thus, where applicable, Eq. (37) leads to

$$\mathbf{N} = \begin{cases} 3\bar{C}\dfrac{\boldsymbol{\Sigma}'}{\bar{\sigma}^2} + \dfrac{2}{3}(g+1)(g+f)\dfrac{\kappa}{\bar{\sigma}}\sinh\left(\kappa\dfrac{\Sigma_{\mathrm{m}}}{\bar{\sigma}}\right)\mathbf{I}, & \mathcal{F} = \bar{\mathcal{F}}^{\mathrm{H}} \\ \dfrac{2}{\mathcal{Y}^2}\mathrm{sgn}\left(\Sigma_{\mathrm{n}}\right)\langle\!\langle |\Sigma_{\mathrm{n}}| - S \rangle\!\rangle \mathbf{n}\otimes\mathbf{n} + \dfrac{1}{\mathcal{T}^2}\left[\mathbf{n}\otimes\boldsymbol{\Sigma}\mathbf{n} + \boldsymbol{\Sigma}\mathbf{n}\otimes\mathbf{n} - 2\Sigma_{\mathrm{n}}\mathbf{n}\otimes\mathbf{n}\right], & \mathcal{F} = \bar{\mathcal{F}}^{\mathrm{I}} \end{cases} \tag{38}$$

where $\mathbf{n}$ is either a principal stress direction or determined in terms of principal stresses using (32) and (29).

3.2. Evolution of porosity

Porosity is defined by the void volume fraction f and the average void aspect ratio w. Since plastic flow in the matrix is isochoric, the evolution of f is given by the usual relation:

$$\frac{\dot{f}}{1-f} = \mathrm{tr}\,\mathbf{D}^p = \dot{\Lambda} N_{kk} \tag{39}$$

The evolution of the void aspect ratio w follows the procedure of Gologanu et al. (1993) whereby the rate of w is identified with the ensemble average of the rates of individual voids, such that

$$\frac{\dot{w}}{w} = \left(\frac{1-3\alpha_1}{f} + 3\alpha_2 - 1\right) D^p_{kk} \qquad \text{when } \mathcal{F} = \bar{\mathcal{F}}^{\mathrm{H}} \tag{40}$$

where $\alpha_1(w)$ is a function of w alone (Keralavarma and Benzerga, 2010). Eq. (40) is a crude estimate but the above result is consistent with the assumption of persistent isotropy. Better estimates would predict the development of preferred orientations, but the induced texture would render the model anisotropic and the analysis of Lode effects impossible. For spherical voids, $\alpha_1 = \alpha_2 = 1/3$ and $\dot{w} = 0$.

Consistent with the above estimate, the evolution of w under inhomogeneous yielding is taken to follow a similar form:

$$\frac{\dot{w}}{w} = \left(\frac{1-3\alpha_1}{f} + 3\alpha_2 - 1\right) \frac{D^p_{kk}}{c} \qquad \text{when } \mathcal{F} = \bar{\mathcal{F}}^{\mathrm{I}} \tag{41}$$

where the plastic strain rate in the ligaments is used instead of the overall strain rate, the parameter $c = \left(\frac{3}{2}\frac{f}{w}\right)^{1/3}\sqrt{\frac{w^2+1}{2}}$ being the ligament volume fraction in volumetric average sense obtained in a similar fashion to $\bar{w}$ elucidated in Appendix A. An alternative approach, which is a priori more consistent, involves expressing plastic incompressibility in the band, yielding an equation similar to (39) for f_{b} with D_{kk} replaced with the mean rate of deformation in the band, D_{kk}/c. However, such an approach relies heavily on the surrogate parameters of Appendix A.

3.3. Strain hardening

Strain hardening is incorporated by writing the flow stress of the matrix $\bar{\sigma}$ as a function of an average plastic strain, $\bar{\epsilon}$, in the matrix, whose rate of evolution is determined from the equality of the plastic dissipation rate at the micro- and macro-scales, which yields the condition

$$\dot{\bar{\epsilon}} = \frac{\boldsymbol{\Sigma} : \mathbf{D}^p}{(1-f)\bar{\sigma}} \tag{42}$$

A power law hardening relation is assumed in all calculations, which takes the form

$$\bar{\sigma}(\bar{\epsilon}) = \sigma_0 \left(1 + \frac{\bar{\epsilon}}{\epsilon_0}\right)^N \tag{43}$$

4. Failure criterion

Under tensile loading, the transition from homogeneous to inhomogeneous yielding constitutes a reasonable definition of ductile failure. That is precisely what has been referred to in the literature as the onset of void coalescence (Benzerga, 2002). The material element undergoes, at the transition, an abrupt drop in stress carrying capacity so that the post-transition deformation is relatively small. For axisymmetric tension, the lower the stress triaxiality the more relevant this measure of failure.

By way of contrast, under combined tension and shear, inhomogeneous yielding may set in quite early. In fact, it is the preferred mechanism under shear-dominated loading in the absence of hardening (Torki and Benzerga, 2018). Yet, the material element retains much load bearing capacity, and failure may not ensue until much larger strains, say by void impingement. Under such circumstances, therefore, failure may not be identified with the onset of – or transition to – inhomogeneous yielding. Hence, for combined tension and shear, a failure criterion by plastic instability is employed here.

For a general class of elasto-plastic materials, the criterion for the onset of a macroscopic instability was derived by Rice (1976), who analyzed the conditions of strain localization into a planar band with unit normal $\mathbf{q}$. Their condition reads in terms of the acoustic tensor $\mathbf{A}$ (Hadamard, 1903)

$$\det \mathbf{A}(\mathbf{q}) = 0; \qquad \mathbf{A}(\mathbf{q}) = \mathbf{q} \cdot \mathbb{C}^t \mathbf{q} \tag{44}$$

where $\mathbb{C}^t$ is the elasto-plastic tangent stiffness tensor, to be evaluated for the constitutive model of the previous section.

Using a porous material yield criterion similar to the multi-surface criterion (36), Vishwakarma and Keralavarma (2019) showed that the localization condition (44) is generally satisfied after the onset of inhomogeneous yielding, irrespective of loading path. They also showed that the normal to the localization band coincides with the normal to the plastic band for inhomogeneous yielding:

$$\mathbf{q} = \mathbf{n} \tag{45}$$

In implementing (44), it is sufficient, therefore, to compute the tangent moduli for a constitutive relation that solely accounts for inhomogeneous yielding. One advantage of this approach is to elude difficulties associated with the (artificial) corners associated with homogeneous to inhomogeneous yield transitions. More recently, Keralavarma et al. (2020) used this result to derive a criterion for failure by instability assuming a specific model for inhomogeneous yielding that did not account for void shape effects. Here, we adapt their result to a general class of yield models.

Criteria of inhomogeneous yielding, such as that presented in Section 2.2 and that in Appendix C, can be written in the following general form (dropping the bar for convenience from $\bar{\mathcal{F}}^{\mathrm{I}}$ and redefining the arguments for the purpose of analysis)

$$\mathcal{F}^{\mathrm{I}}(\Sigma_{\mathrm{n}}, \Sigma_{\mathrm{sh}}, \boldsymbol{\alpha}) = 0 \tag{46}$$

where $\Sigma_{\mathrm{n}} = \mathbf{n} \cdot \boldsymbol{\Sigma}\mathbf{n}$ and $\Sigma_{\mathrm{sh}} = \sqrt{\mathbf{n} \cdot \boldsymbol{\Sigma}^2\mathbf{n} - \Sigma_{\mathrm{n}}^2}$ are the normal and shear stresses on the plane of inhomogeneous yielding, and $\boldsymbol{\alpha}$ is a vector collecting internal state variables (here f and w). The plastic flow direction is given by:

$$\mathbf{N} = \mathcal{F}^{\mathrm{I}}_{\mathrm{n}} \mathbf{n} \otimes \mathbf{n} + \frac{1}{2}\mathcal{F}^{\mathrm{I}}_{\mathrm{sh}}(\mathbf{m} \otimes \mathbf{n} + \mathbf{n} \otimes \mathbf{m}) \tag{47}$$

where $\mathcal{F}^{\mathrm{I}}_{\mathrm{n}} = \partial\mathcal{F}^{\mathrm{I}}/\partial\Sigma_{\mathrm{n}}$ and $\mathcal{F}^{\mathrm{I}}_{\mathrm{sh}} = \partial\mathcal{F}^{\mathrm{I}}/\partial\Sigma_{\mathrm{sh}}$ are shorthand notations and $\mathbf{m}$ is the unit vector along the direction of the resolved shear traction on the plastic band with normal $\mathbf{n}$. The elasto-plastic tangent modulus $\mathbb{C}^t$ is then expressed as

$$\mathbb{C}^t = \mathbb{C} - \frac{1}{D}(\mathbb{C} : \mathbf{N}) \otimes (\mathbb{C} : \mathbf{N}), \qquad D = \mathbf{N} : \mathbb{C} : \mathbf{N} - \frac{\partial \mathcal{F}^{\mathrm{I}}}{\partial \boldsymbol{\alpha}} \cdot \boldsymbol{\mathscr{Q}} \tag{48}$$

with $\boldsymbol{\mathscr{Q}}$ defined through $\dot{\boldsymbol{\alpha}} = \dot{\lambda}\boldsymbol{\mathscr{Q}}$ using the plastic multiplier as above. Note that $\boldsymbol{\mathscr{Q}}$ is not necessarily equal to $\partial F^I/\partial\boldsymbol{\alpha}$ (associativity does not necessarily hold for the evolution law of the internal parameters collectively denoted $\boldsymbol{\alpha}$.)

Substituting (47) and (48) into $(44)_2$, and using $\mathbb{C} = 2\mu\mathbb{I} + \lambda\mathbf{I} \otimes \mathbf{I}$ for isotropic elasticity with λ and μ the Lamé constants, yields

$$\begin{aligned}\mathbf{A}(\mathbf{n}) = \mu\mathbf{I} - \frac{1}{D}\mu^2(\mathcal{F}^{\mathrm{I}}_{\mathrm{sh}})^2 \mathbf{m} \otimes \mathbf{m} + \left[(\lambda+\mu) - \frac{1}{D}(\lambda+2\mu)^2(\mathcal{F}^{\mathrm{I}}_{\mathrm{n}})^2\right] \mathbf{n} \otimes \mathbf{n} \\ - \frac{1}{D}\mu(\lambda+2\mu)\mathcal{F}^{\mathrm{I}}_{\mathrm{n}}\mathcal{F}^{\mathrm{I}}_{\mathrm{sh}}(\mathbf{m} \otimes \mathbf{n} + \mathbf{n} \otimes \mathbf{m})\end{aligned} \tag{49}$$

whose determinant evaluates to

$$\det \mathbf{A}(\mathbf{n}) = \frac{1}{D}\mu^2(\lambda+2\mu)\left[D - \mu(\mathcal{F}^{\mathrm{I}}_{\mathrm{sh}})^2 - (\lambda+2\mu)(\mathcal{F}^{\mathrm{I}}_{\mathrm{n}})^2\right] \tag{50}$$

with D in $(48)_2$ now given by:

$$D = \mu(\mathcal{F}^{\mathrm{I}}_{\mathrm{sh}})^2 + (\lambda+2\mu)(\mathcal{F}^{\mathrm{I}}_{\mathrm{n}})^2 - \frac{\partial \mathcal{F}^{\mathrm{I}}}{\partial \boldsymbol{\alpha}} \cdot \boldsymbol{\mathscr{Q}} \tag{51}$$

Using (51) in (50) in $(44)_1$ yields the following failure criterion:

$$-\frac{\partial \mathcal{F}^{\mathrm{I}}}{\partial \boldsymbol{\alpha}} \cdot \boldsymbol{\mathscr{Q}} = 0 \tag{52}$$

which is independent of the elastic constants of the material.

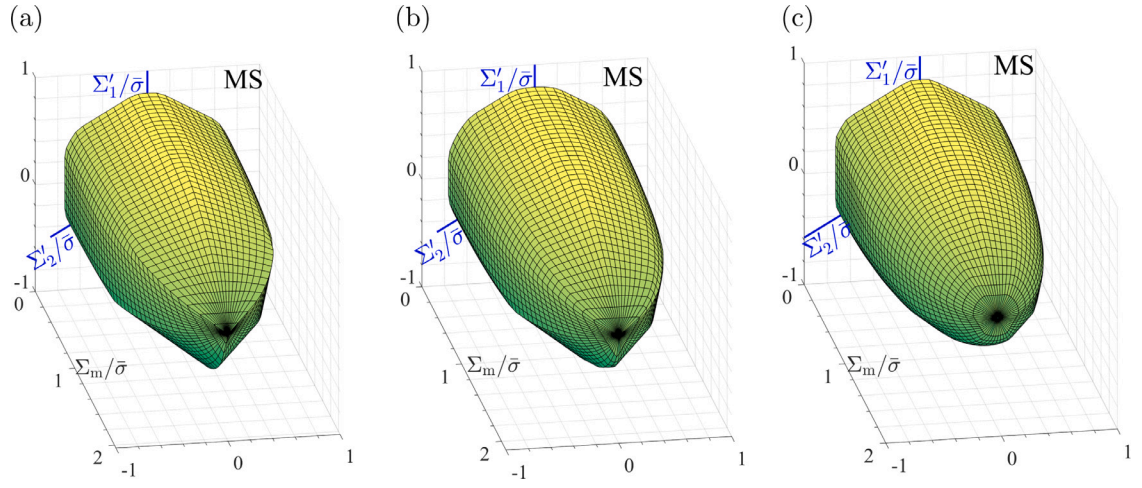

Fig. 2. Effective yield surfaces of a porous material with void volume fraction $f = 0.03$ and three values of the void aspect ratio: (a) $w = 1$, (b) $w = 5$, and (c) $w = 1/5$.

5. Results

Three sets of results are presented. First, general shapes of effective yield surfaces described by Eq. (36), as derived in Section 2, are illustrated for various values of the internal variables f and w. Then, the salient features of the isotropic failure theory are presented, first under the constraint of plane stress then more generally. To this end, the constitutive relations described in Section 3 are integrated for prescribed loading paths using explicit integration of the internal variables and a single-step Runge–Kutta scheme. At any time step, an overall effective strain is defined as $\varepsilon_{\rm eq} = \int \dot{\varepsilon}_{\rm eq} {\rm d}t$ with $\dot{\varepsilon}_{\rm eq} = \sqrt{2/3\,\mathbf{D}^p : \mathbf{D}^p}$, the value of which is found to be not so different from the matrix effective plastic strain $\bar{\varepsilon}$. Calculations are stopped when the localization-based failure criterion (52) is met. Both the strain to failure, $\bar{\varepsilon}^{\rm L}$, and the orientation of the localization band, $\varphi_{\rm c}$, are recorded. Where appropriate, the strain to the onset of inhomogeneous yielding, $\bar{\varepsilon}^{\rm I}$, is also reported. Both IY criteria (16) or (18) were used as basis for (36) and produced similar results but all figures below are shown using (18) to avoid issues associated with singular parts of criterion (16).

5.1. Yield surfaces

Fig. 2 depicts surfaces corresponding to yield criterion (36) for a void volume fraction of 0.03 and three values of the void aspect ratio. The three axes depicted in blue correspond to the principal components of the stress deviator:

$$\Sigma_1' = \frac{2}{3}\Sigma_{\rm eq}\cos\theta, \qquad \Sigma_2' = \frac{2}{3}\Sigma_{\rm eq}\cos\left(\theta - \frac{2\pi}{3}\right), \qquad \Sigma_3' = \frac{2}{3}\Sigma_{\rm eq}\cos\left(\theta + \frac{2\pi}{3}\right) \tag{53}$$

given in terms of the von Mises equivalent stress and the Lode angle, θ. For reference, the third invariant $J_3 = \det\boldsymbol{\Sigma}'$, the Lode parameter L and the Lode angle θ are related through:

$$L = -\cos 3\theta = -\frac{27}{2}\frac{J_3}{\Sigma_{\rm eq}^3} \tag{54}$$

Clearly, the surfaces shown in Fig. 2 depend on θ, hence on J_3. It is also clear from Eq. (14) that the HY (Gurson-like) criterion only depends on $\Sigma_{\rm m}$ and $\Sigma_{\rm eq}$. Thus, any dependence upon J_3 must originate from the inhomogeneous yield criterion, Eq. (34). As discussed in Appendix D, internal necking alone implies J_3-dependence. For completeness, the HY and IY surfaces are plotted separately in Appendix D for the $w = 1/5$ case.

The $w = 1$ surface, Fig. 2a, has a vertex on the hydrostatic axis, which is associated with the indeterminacy of the plastic band orientation under inhomogeneous yielding. This is a high-order vertex in the sense that any meridian section would exhibit the vertex. On the other hand, the vertex is of lower order in the $w = 5$ surface, Fig. 2b, in the sense that the vertex disappears for certain types of loading, to be specified below. This phenomenon is associated with homogeneous yielding being favored for such loadings, in which case the normal to the yield surface is determined. By way of contrast, the vertex on the hydrostatic axis disappears completely in the $w = 1/5$ surface, Fig. 2c. Here, homogeneous yielding is found to be the active mode at very high stress triaxiality. In order to understand these features, octahedral and meridian sections of the surfaces must first be analyzed.

Fig. 3 shows octahedral plane sections of the surfaces in Fig. 2 for various amounts of hydrostatic stress. The restriction of the yield function to the unit circle is $\frac{2\pi}{3}$–periodic and symmetric about the bisector over any period. Hence, it is fully determined by its restriction to the θ interval $[0, \pi/3]$. On the π-plane (Fig. 3a) inhomogeneous yielding is preferred for shear-dominated states (θ about $\pi/6$) whereas homogeneous yielding activates near axisymmetric states, either with a major axial stress ($\theta \sim 0$ or $L \sim -1$) or a minor axial stress ($\theta \sim \pi/3$ or $L \sim +1$). This results in a Lode dependence of effective yield, which carries over much of the range of

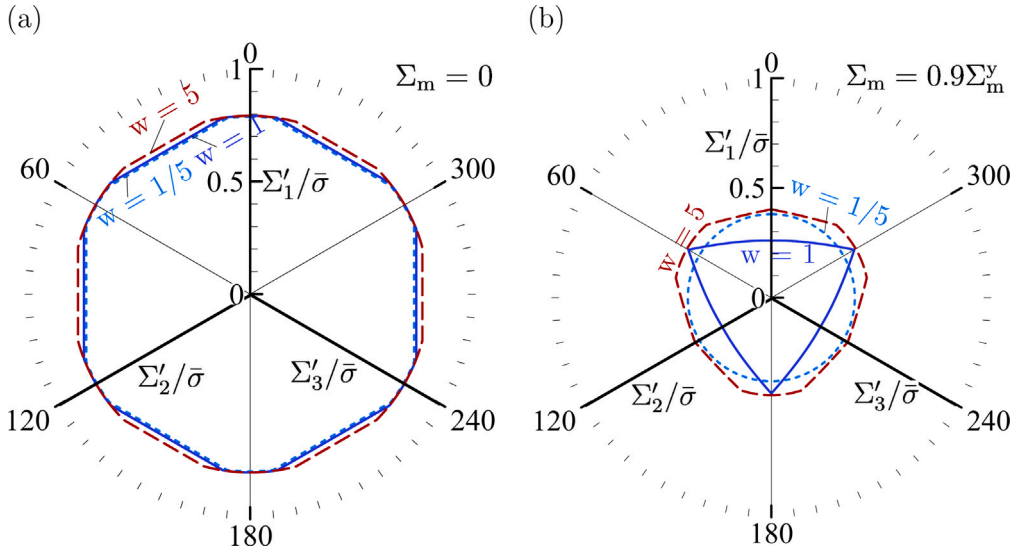

Fig. 3. Octahedral sections of the yield surfaces in Fig. 2 for $f = 0.03$ and three values of the void aspect ratio w at: (a) $\Sigma_m = 0$, (b) $\Sigma_m = 0.9\Sigma_m^y$.

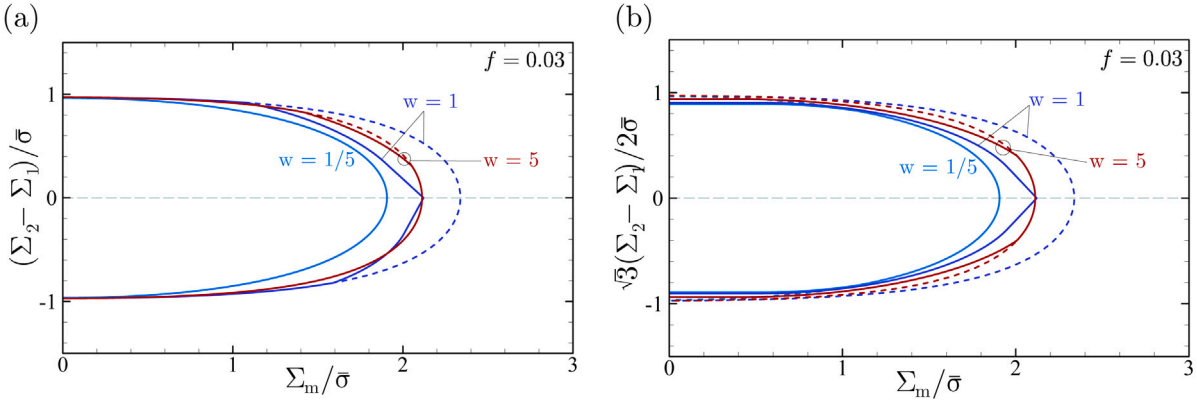

Fig. 4. Meridian sections of HY surfaces (dashed) and effective yield surfaces (solid) for $f = 0.03$ and three values of w: (a) axisymmetric loadings ($|L| = 1$, *i.e.* $\theta = 0$ or $\theta = \pi/3$); (a) generalized shear ($L = 0$, *i.e.* $\theta = \pi/6$).

Σ_m. Of particular interest is the shape of the *nose* of the yield surface for large values of superposed hydrostatic stress, Fig. 3b. The entirety of the $w = 1$ surface is governed, in this case, by IY whereas the $w = 5$ surface exhibits HY portions (near $L = +1$), hence the lower-order of the vertex on the hydrostatic axis. On the other hand, the entire section of the $w = 1/5$ surface is dominated by HY, which leads to Lode independence at very high triaxiality.

Fig. 4 shows meridian sections of the effective yield surfaces of Fig. 2. For comparison, corresponding sections of the Lode-independent HY surfaces are shown dashed. For spherical voids, the vertex on the hydrostatic axis is observed under both axisymmetric loadings ($|L| = 1$; Fig. 4a) and generalized plane strain or shear ($L = 0$; Fig. 4b). As noted before, this is because inhomogeneous yielding is predicted for pure hydrostatic loading. However, the situation changes for non-spherical voids. For the internal parameter values chosen here, (vertex-free) homogeneous yielding is predicted for $w = 1/5$ regardless of the value of L. No vertex is seen for $w = 5$ in Fig. 4, but for other loading paths (that are neither axisymmetric nor plane strain) the vertex may still be approached; see Fig. 2b.

The above trends clearly depend on the competition between homogeneous versus inhomogeneous yielding. Under hydrostatic loading, the yield stress for HY is obtained from (14):

$$\Sigma_m^y = -\frac{1}{\kappa}\bar{\sigma}\ln\frac{g+f}{g+1} \tag{55}$$

For prolate voids $w \geq 1$, $g = 0$ and the above limit reduces to $-1/\kappa\,\bar{\sigma}\ln f$. Thus, for prolate voids the yield stress under hydrostatic loading decreases monotonically with increasing void elongation since κ increases with w; see Fig. 34 of Benzerga and Leblond (2010). For spherical voids, $\kappa = 3/2$ such that Hill's (1950) exact solution for a hollow sphere is recovered. For oblate voids, the

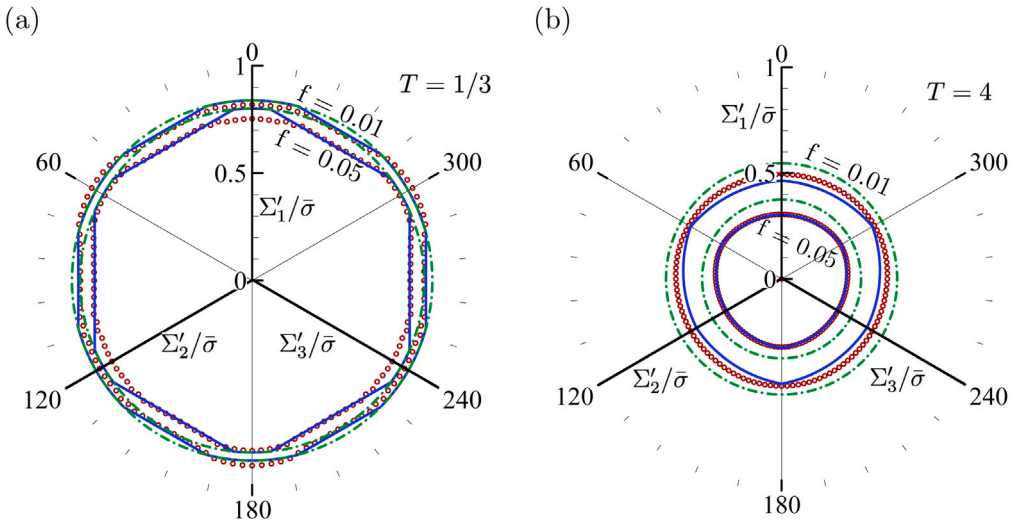

Fig. 5. Comparison of multisurface theory (solid lines) with numerical limit analysis (points) in terms of octahedral plane projections of the intersection of the yield surface with the cone of constant triaxiality for two values of the void volume fraction f: (a) $T = 1/3$, (b) $T = 4$. HY surfaces (dashed) are also shown for reference.

value taken by g plays a key role, which usually reverses the trend such that in all cases the yield stress is largest for spherical voids. This explains the non-monotonic ordering of yield stresses on the hydrostatic axis for HY (dashed).

The effect of void shape on inhomogeneous yielding is straightforward, considering that the surrogate aspect ratio is linear in w, within the range considered; see Eq. (A.5), which shows the trend more clearly than (22). It has long been known that the coalescence stress is a decreasing function of w (Benzerga, 2002). This results directly from $(17)_2$, with the outcome being that the yield stresses under hydrostatic loading rank order according to the value of w. The combination of the above two trends (effect of w on the HY and IY limits in hydrostatic loading) results in the final ordering seen in Fig. 4 for the effective values of $\Sigma_{\mathrm{m}}^{\mathrm{y}}$.

The fact that there is no vertex for some ($w = 5$) or all ($w = 1/5$) ways to approaching the hydrostatic axis does not mean that the corresponding yield surfaces are corner-free (see Fig. 2). Indeed, all surfaces exhibit the two types of corners described in Section 3.

At low stress triaxiality, homogeneous yielding is dominant under axisymmetric loading (Fig. 4a) whereas inhomogeneous yielding prevails under generalized shear (or plane strain) loading (Fig. 4b). Interestingly, the $w = 1/5$ surface is almost entirely dominated by homogeneous yielding. Exceptions include very high triaxialities for $L = -1$ and very low triaxialities for $L = 0$.

The latter case corresponds to shear-dominated loading, which is of particular interest. In the limit of simple or pure shear ($\Sigma_{\mathrm{m}} = 0$ and $L = 0$), the yield stresses for HY and IY are $\tau = (1 - f)\bar{\tau}$ and $\tau = (1 - f_{\mathrm{b}})\bar{\tau}$, respectively from (14) and (34). Because the band porosity is larger than the overall porosity, inhomogeneous yielding is always favored under shear loading.

Not every quantitative aspect of the effective yield surfaces shown in Figs. 2–4 can be taken for granted. A full assessment of the isotropic criterion requires numerical estimates of limit loads for multi-void dispersions with random void orientations. Such calculations are still not available. However, since one finding is that the Lode-dependence of effective yield at low triaxiality is weakly dependent upon the void aspect ratio, it suffices to assess the model for a dispersion of spherical voids to give some credence to the predictive capability of the new criterion. This problem has been approached by Keralavarma (2017) by means of finite element based limit analyses of single-void unit cells using a technique initially developed by Madou and Leblond (2012). The numerical results are used to calibrate (34) using $b = 0.95$; see Appendix B.

Fig. 5 compares the results of the multisurface criterion and the finite element results for two values of f. Since the numerical yield loci are typically approached using proportional loadings (*i.e.* fixed values of T and L) what is shown in the figure are actually intersections of yield loci with a cone of constant triaxiality. The HY results are also shown dashed for the sake of comparison.

The key observation in Fig. 5 is that the numerical yield loci exhibit non-negligible Lode dependence especially at $T = 1/3$, in keeping with the predictions of the multisurface theory, as pointed out earlier by Keralavarma (2017). The transitions between the various sectors are smooth in the numerical loci, albeit with strong curvature.

Next, Fig. 6 shows corresponding meridian sections for axisymmetric loading ($L = \pm 1$) and generalized shear ($L = 0$). The quasi-vertex on the hydrostatic axis is clearly visible in the numerical yield loci. Also, the numerical results clearly show that the limit in shear is governed by inhomogeneous yielding. This is barely visible for $f = 0.01$ (Fig. 6c) but becomes clear for $f = 0.05$ (Fig. 6d). Note that the upper-bound character of the multisurface model cannot be assessed directly using this set of numerical results. Indeed, the meso-scale model employs a cylindrical cell embedding a co-axial cylindrical void of unit aspect ratio, whereas the finite element results are for a spherical void inside a cubic cell. Discrepancies of this sort have been discussed by Torki et al. (2017).

The essential features of the multisurface yield theory were included in the prequel. Figs. 7 and 8 provide additional details on the effect of void volume fraction in octahedral and meridian projections, respectively. In Fig. 7 notice first that, with increasing

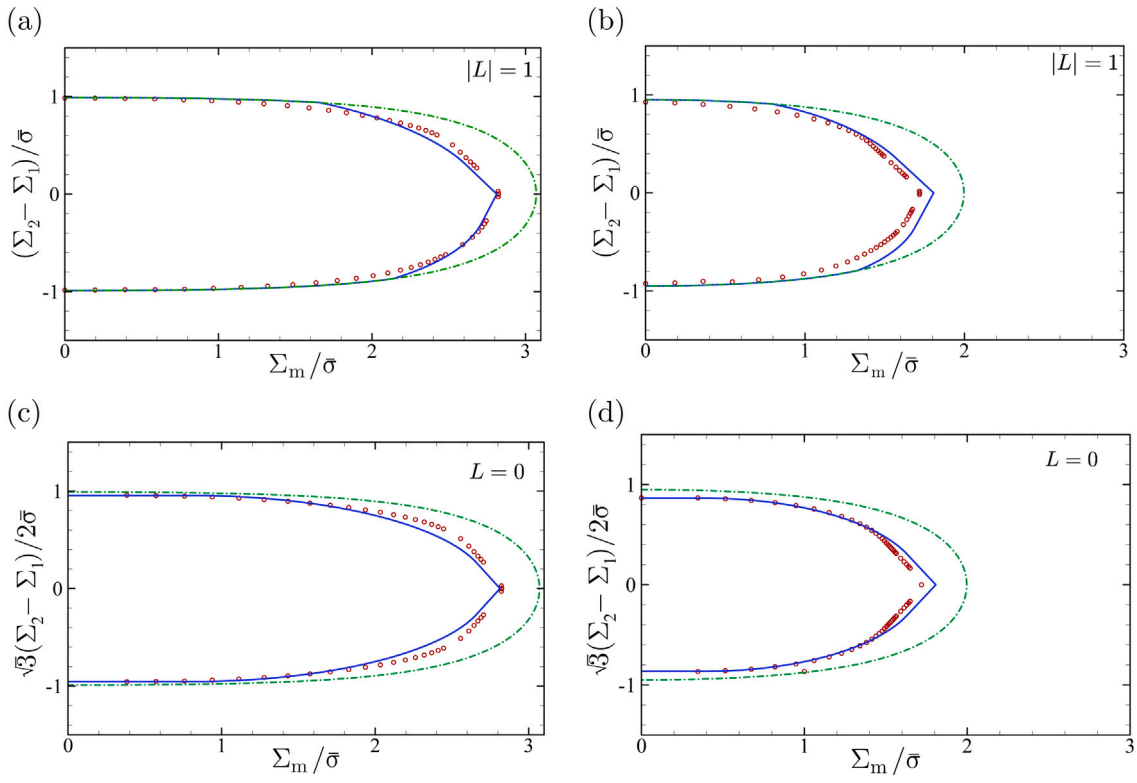

Fig. 6. Comparison of multisurface theory (solid lines) with numerical limit analysis (points) in meridian sections of yield surfaces: (a) $|L| = 1$ and $f = 0.01$; (b) $|L| = 1$ and $f = 0.05$; (a) $L = 0$ and $f = 0.01$; (b) $L = 0$ and $f = 0.05$. HY surfaces (dashed) are also shown for reference.

amounts of hydrostatic stress, the yield surface gradually evolves from a six-fold to a three-fold symmetry; compare (a) and (b) on the one hand with (c) on the other hand. At $T = 1$ for instance, Fig. 7c, yielding is predicted to be inhomogeneous for axisymmetric loading with a major axial stress ($\theta = 0$; $L = -1$) but homogeneous with a major lateral stress ($\theta = \pi/3$; $L = +1$). This point merits further discussion; see Appendix D. With increasing porosity, the HY surface shrinks at a slower rate than the IY surface. This is illustrated in Fig. 7d.

Meridian projections corresponding to Fig. 7 are shown in Fig. 8. They illustrate the large difference between HY and effective surfaces at moderate to high triaxialities, in addition to the vertex on the hydrostatic axis, as previously shown. It is emphasized that in the dilute limit ($f \to 0$) the relative order of the HY and IY limits under pure hydrostatic loading is reversed (not shown).

5.2. Plane stress failure loci

Consider states of plane stress, say in the $\mathbf{e}_1$–$\mathbf{e}_2$ principal plane, with $\Sigma_1 \geq \Sigma_2$. Let $\rho = \Sigma_2/\Sigma_1$ be the biaxiality ratio. Then the stress triaxiality and Lode parameter, which are given by:

$$T = \frac{1}{3}\mathrm{sgn}\left(\Sigma_1\right)\frac{\rho+1}{\sqrt{\rho^2-\rho+1}} \tag{56}$$

and

$$L = \frac{1}{2}\frac{(1+\rho)(2-\rho)(2\rho-1)}{(\rho^2-\rho+1)^{3/2}} \tag{57}$$

are not independent. Unlike for axisymmetric stress states ($|L| = 1$) or generalized shear ($L = 0$), the Lode parameter varies within its full range in plane stress ($-1 \leq L \leq +1$). In addition, the full range is spanned for any of the following three biaxiality regimes: biaxial tension ($0 \leq \rho \leq 1$), biaxial compression ($\rho \geq 1$), and generalized plane shear ($\rho \leq 0$).

The constitutive relations described in Section 3 are integrated for a prescribed value of ρ and the output quantities of interest are $\bar{\epsilon}^{\mathrm{L}}$, φ_{c} and $\bar{\epsilon}^{\mathrm{I}}$.

Fig. 9 shows the predicted failure locus for proportional loading paths corresponding to initially spherical voids ($w_0 = 1$) with $f_0 = 0.001$. Focus is laid on $T \geq 0$. Remarkably, the locus exhibits key features of experimental loci reported by Bao and Wierzbicki (2004) and Bai and Wierzbicki (2010) among others. First, there is a cusp at $T = 1/3$, which corresponds to the maximum ductility predicted under biaxial tension. Also, there are two local minima, one under biaxial tension ($1/3 \leq T \leq 2/3$) and one under

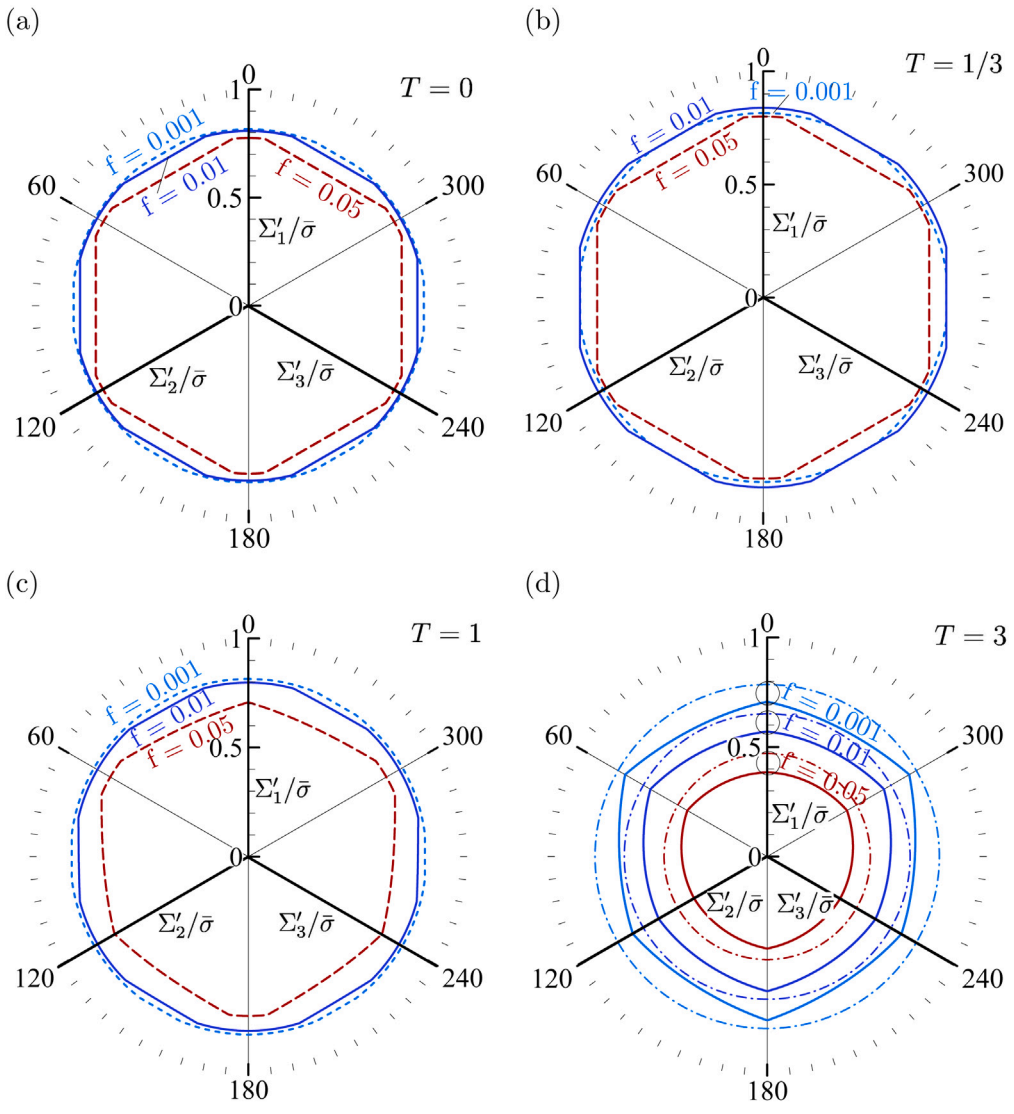

Fig. 7. Effect of void volume fraction f on octahedral projections of effective yield surfaces for: (a) $T = 0$, (b) $T = 1/3$, (c) $T = 1$, (d) $T = 3$. In (d) the HY surfaces are shown for reference (see text.)

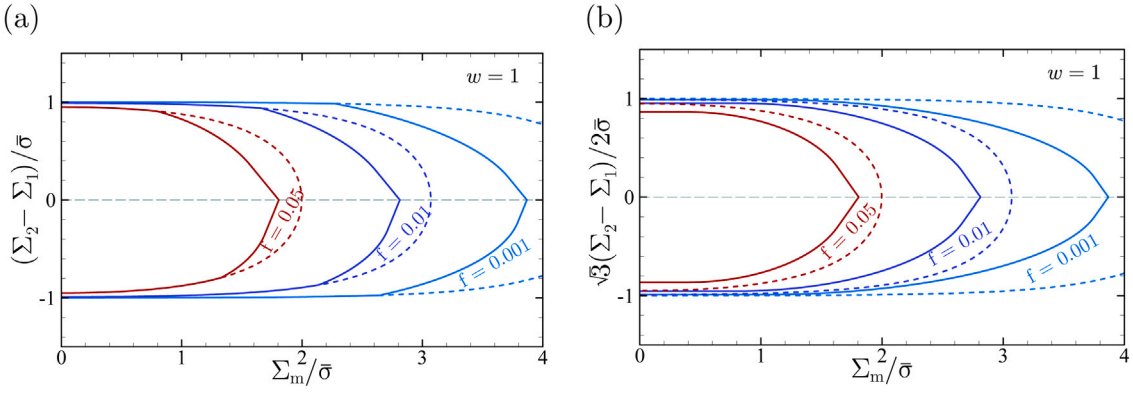

Fig. 8. Effect of void volume fraction f on meridian sections of effective yield surfaces for: (a) axisymmetric loadings, $|L| = 1$ and (b) generalized shear, $L = 0$. HY surfaces are shown dashed for reference.

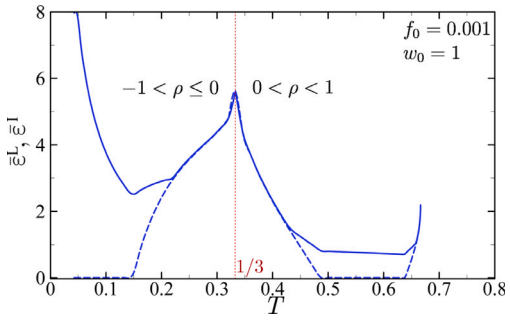

Fig. 9. Strain to failure, $\bar{\varepsilon}^L$, (solid lines) and inhomogeneous yield strain, $\bar{\varepsilon}^I$, (dashed) versus stress triaxiality, T, under plane stress loading for $f_0 = 0.001$ and $w_0 = 1$.

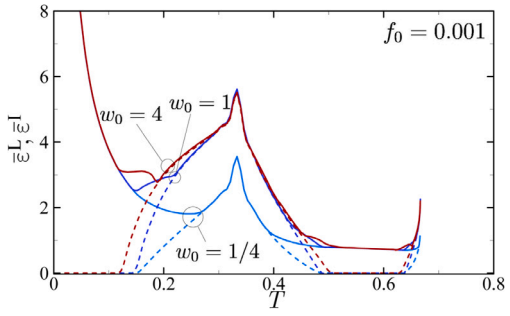

Fig. 10. Failure loci (solid) and inhomogeneous yield loci (dashed) under plane stress loading for $f_0 = 0.001$ and three values of the initial void aspect ratio w_0.

generalized shear ($0 \leq T \leq 1/3$), the former being the global minimum. An essential difference, however, with experimental loci is that the shear ductility is found to be infinite. This feature appears to be rooted in the isotropic character of the theory and merits further discussion below. For uniaxial tension ($T = 1/3$), failure occurs by internal necking normal to the applied stress. Internal necking is also found to prevail under equi-biaxial tension, but the orientation is undetermined. In all other cases, failure occurs under combined tension and shear along a plane at an angle φ_c between 42.5° and 45° from a principal direction.

Fig. 10 shows the effect of the initial void aspect ratio on predicted failure loci for $f_0 = 0.001$. The $w_0 = 1$ and $w_0 = 4$ failure loci are very close to each other and the main effect of initial void shape appears to manifest for initially flat voids ($w_0 = 1/4$). The overall shape of the locus remains the same but two things are affected by w_0: the uniaxial ductility (for $T = 1/3$) and the minimum ductility between pure shear and uniaxial tension. On the other hand, while the locus is altered in the biaxial tension regime ($0 \leq \rho \leq 1$, *i.e.*, $1/3 \leq T \leq 2/3$) the minimum ductility is not affected by the value of w_0 over the range of values considered here. The pure shear ductility is predicted to be infinite, irrespective of the value of w_0.

Failure loci such as those shown in Figs. 9 and 10 do not appear to have been predicted previously based on first principles. They bear direct connection to apparent fracture loci determined experimentally in various studies. In order to understand the general shapes of plane stress failure loci, a deeper analysis of intrinsic failure loci is necessary.

5.3. *Intrinsic failure loci*

More general loading paths are considered by independently prescribing values for the triaxiality T and Lode parameter L. The failure loci in plane stress (Figs. 9 and 10) cannot be regarded as "intrinsic" in that the Lode parameter varies along each curve. Here, failure loci are constructed under proportional loading, which are called intrinsic in that they serve as a basis for interpreting failure loci obtained under plane stress or non-proportional paths.

Fig. 11 shows that the onset of inhomogeneous yielding (dashed lines) always precedes strain localization (solid lines). This is given, based on (45), but it is easily checked that strain localization would not occur earlier should one assume HY criterion (14) alone. This is important because the opposite view has erroneously pervaded in the recent literature; see *e.g.* Mohr and Marcadet (2015). For nearly axisymmetric stress states ($|L| \sim 1$), failure by strain localization occurs immediately after the transition to inhomogeneous yielding, Fig. 11a,b. The behavior at very high triaxiality (*e.g.* $T = 3$ in Fig. 11c) appears as an exception only because of the smaller magnitudes of accumulated strains. On the other hand, for stress states near generalized shear ($L = 0$) the IY mode of deformation dominates from the outset of plastic flow and the distance between $\bar{\varepsilon}^I$ and $\bar{\varepsilon}^L$ can be quite significant, particularly at low triaxiality.

What is of particular importance is that Fig. 11 demonstrates the predicted effect of the Lode parameter on the strain to failure $\bar{\varepsilon}^L$, irrespective of triaxiality level or initial porosity content. Every failure locus $\bar{\varepsilon}^L(L)$ has three features: (i) it is not symmetric about

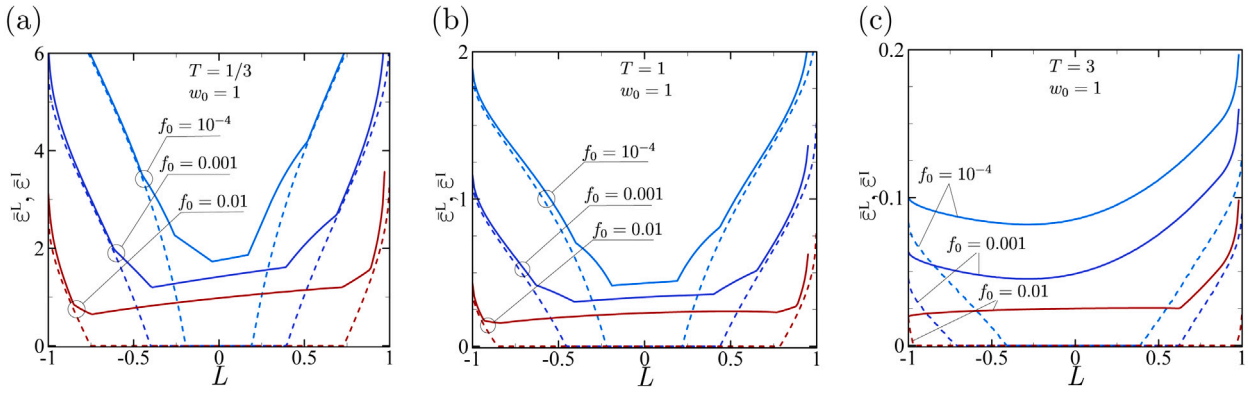

Fig. 11. Strain to failure, $\bar{\varepsilon}^L$, (solid lines) and inhomogeneous yield strain, $\bar{\varepsilon}^I$, (dashed) versus Lode parameter, L, for three values of the initial void volume fraction, f_0, of spherical voids: (a) for $T = 1/3$, (b) $T = 1$, (c) $T = 3$.

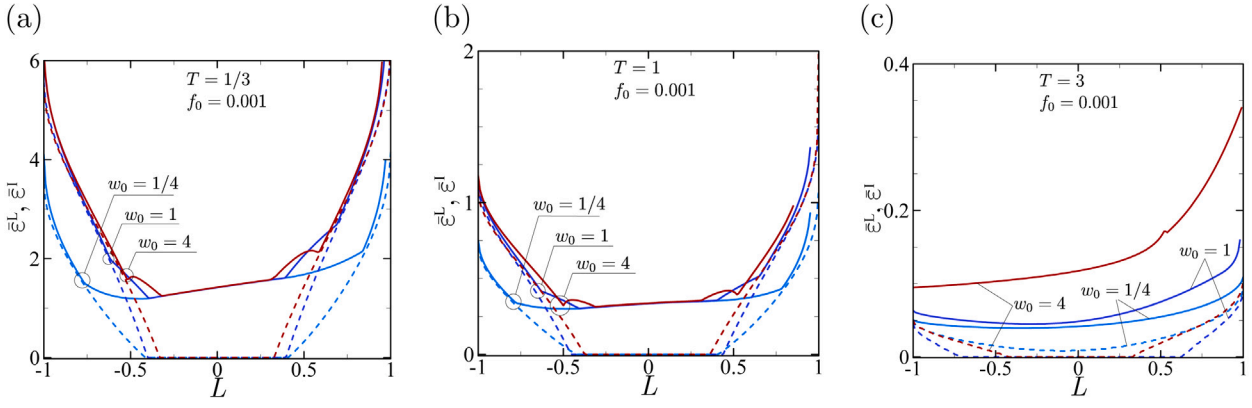

Fig. 12. Strain to failure, $\bar{\varepsilon}^L$, (solid lines) and inhomogeneous yield strain, $\bar{\varepsilon}^I$, (dashed) versus Lode parameter, L, for $f_0 = 0.001$ and three values of the initial void aspect ratio, w_0: (a) for $T = 1/3$, (b) $T = 1$, (c) $T = 3$.

$L = 0$; (ii) The strain to failure is always higher under generalized compression ($L = +1$) than under generalized tension ($L = -1$); and (iii) the minimum ductility lies somewhere between generalized shear ($L = 0$) and generalized tension. This minimum moves farther away from the state of generalized shear as either the void volume fraction or the triaxiality increase. These trends are all consistent with cell model calculations (Dunand and Mohr, 2014; Vishwakarma and Keralavarma, 2019).

The effect of the Lode parameter on the strain to failure shown in Fig. 11 is rooted in the Lode-dependence of the multisurface yield criterion (36), as illustrated in Section 5.1. This is evident when failure occurs immediately after inhomogeneous yielding (regimes where solid and dashed lines are close to each other). For states near generalized shear ($L = 0$) one contribution to Lode-dependence comes from the yield surface itself (when IY is active), but an additional contribution comes from the strain localization condition. Regardless, the Lode effect is not as strong for such states as it is near $|L| = 1$.

Fig. 12 illustrates the effect of the initial void aspect ratio w_0 on failure loci for $f_0 = 0.001$. Near generalized shear states ($L = 0$) the effect of w_0 is only noticeable at very high triaxiality (Fig. 12c) with the $w_0 = 4$ locus being distinctly above the other two. On the other hand, near axisymmetric stress states ($|L| = 1$) the $w_0 = 1/4$ failure locus lies significantly below the other two, especially at low (Fig. 12a) to moderate (Fig. 12b) triaxiality.

Fig. 13 shows the strain to failure versus stress triaxiality for the two benchmark values of L (-1 and 0). Three sets of results are shown, which correspond to values of the initial void volume fraction spanning three orders of magnitude. Likewise, Fig. 14 depicts the effect of the initial void aspect ratio under both generalized tension (Fig. 14a) and generalized shear (Fig. 14b). As above, the dashed curves represent the $\bar{\varepsilon}^I$ versus T curves. Under generalized shear (Figs. 13b and 14b) the dashed lines lie on the horizontal axis since inhomogeneous yielding prevails from the outset.

The key observation in Figs. 13 and 14 is that the strain to failure is a monotonically decreasing function of triaxiality, irrespective of Lode parameter, initial void content or shape. Given a triaxiality, an initial void volume fraction and aspect ratio, the ductility under generalized shear is always smaller than under generalized tension although the shear ductility is not the absolute minimum, as previously shown in Figs. 11 and 12. An order-of-magnitude increase in f_0 can lead to a significant reduction in ductility (above a unit of strain), especially at low triaxiality, Fig. 13. On the other hand, the effect of initial void shape is weaker, Fig. 14, and does not manifest in generalized shear, Fig. 14b.

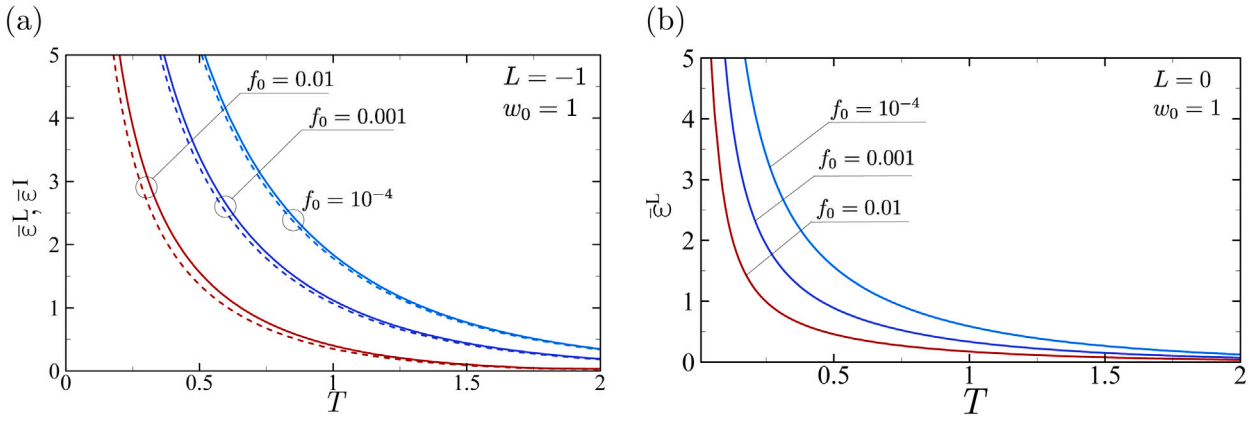

Fig. 13. Strain to failure, $\bar{\varepsilon}^{\mathrm{L}}$, (solid lines) and inhomogeneous yield strain, $\bar{\varepsilon}^{\mathrm{I}}$, (dashed) versus triaxiality, T, for three values of the initial void volume fraction, f_0, of spherical voids: (a) $L = -1$, (b) $L = 0$.

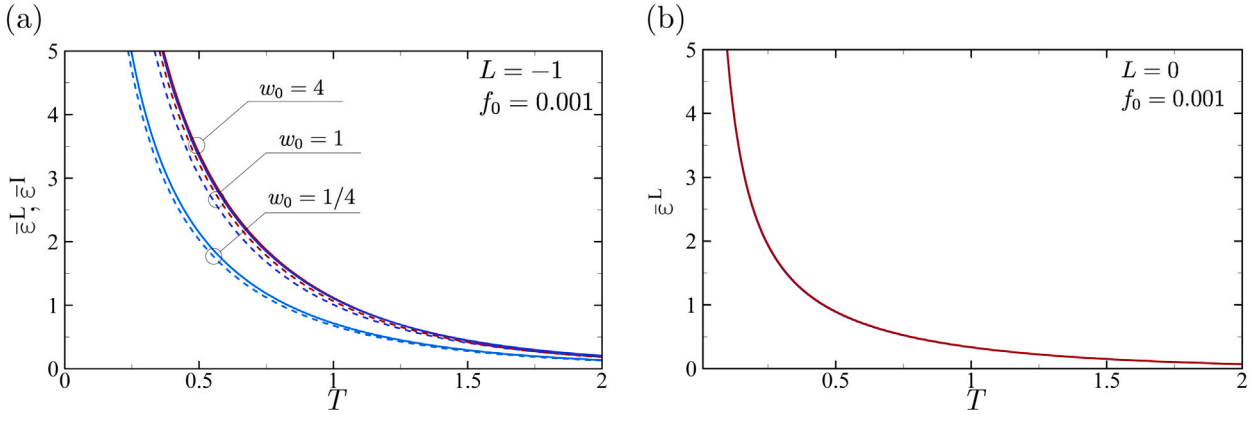

Fig. 14. Strain to failure, $\bar{\varepsilon}^{\mathrm{L}}$, (solid lines) and inhomogeneous yield strain, $\bar{\varepsilon}^{\mathrm{I}}$, (dashed) versus triaxiality, T, for $f_0 = 0.001$ and three values of the initial void aspect ratio, w_0: (a) $L = -1$, (b) $L = 0$.

Every data point on the failure loci of Figs. 11–14 is the result of a computation that produces an effective response along with histories for the internal variables f and w. Figs. 15 and 16 illustrate this for two cases in order to shed light on the effect of w_0 on ductility near axisymmetric states (*e.g.* Fig. 12a,b) and the absence thereof near generalized shear (*e.g.* Fig. 14b).

Fig. 15a shows the overall response in generalized tension at a triaxiality $T = 1$. The three curves correspond to the three values of initial aspect ratio w_0 considered above. For each of the three cases analyzed, an arrow points to the location of the maximum of Σ_{eq}. In each case, there is softening before the onset of inhomogeneous yielding (marked with ∘), which leads to immediate failure (marked by x). While such (material-point level) softening may not be detectable in a structural response, the post peak-stress deformation can be quite significant. In the $w_0 = 4$ case, for example, the amount of post-peak straining adds up to over 0.3.

Fig. 15b depicts the corresponding evolution of the void volume fraction. Recall from (39) that the rate of void growth under homogeneous yielding is proportional to:

$$\dot{f} \propto 2(g+1)(g+f)\frac{\kappa}{\bar{\sigma}}\sinh\left(\kappa\frac{\Sigma_{\mathrm{m}}}{\bar{\sigma}}\right) \tag{58}$$

where due account was taken of $(38)_1$. For prolate voids $g = 0$ and (58) explains the faster rate of void growth in the $w_0 = 4$ case relative to $w_0 = 1$, Fig. 15b, since κ increases with w (see *e.g.* Fig. 34 in Benzerga and Leblond, 2010). The growth rate is enhanced in the $w_0 = 1/4$ case because of the effect of so-called secondary porosity g. For axisymmetric loadings, the transition to inhomogenous yielding is equivalent to the onset of coalescence. The latter occurs at $f/f_0 \approx 30$ for $w_0 = 1$ but for $f/f_0 \approx 40$ for $w_0 = 4$. This is attributed to the fact that the coalescence stress in tension (given by $S + \mathcal{V}$) is a decreasing function of w (Benzerga and Leblond, 2014).

The evolution of the void aspect ratio, depicted in Fig. 15c, is consistent with evolution law (40). Since the $1/f$ term dominates, the sign of $1 - 3\alpha_1$ determines whether the void flattens or elongates. Curves of α_1 versus w may be found in Benzerga (2000) (Fig. IV.11). For much of the history, the void shapes remain distinct from each other. This explains the differences in porosity evolution (Fig. 15b) and, by way of consequence, in the overall response and failure (Fig. 15a).

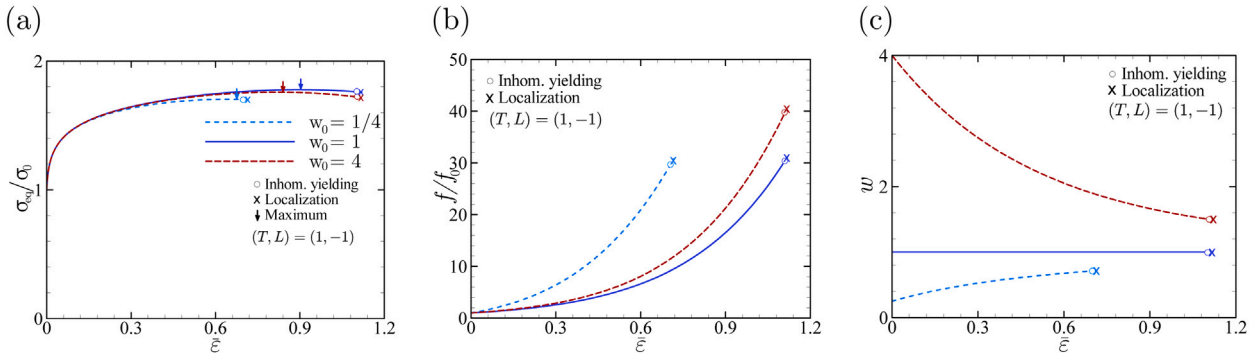

Fig. 15. Overall equivalent stress, Σ_{eq}, normalized by the initial yield stress of the matrix, σ_0 in (43), versus the matrix effective plastic strain, $\bar{\varepsilon}$, for $L = -1$, $T = 1$, $f_0 = 0.001$ and three values of the initial aspect ratio w_0.

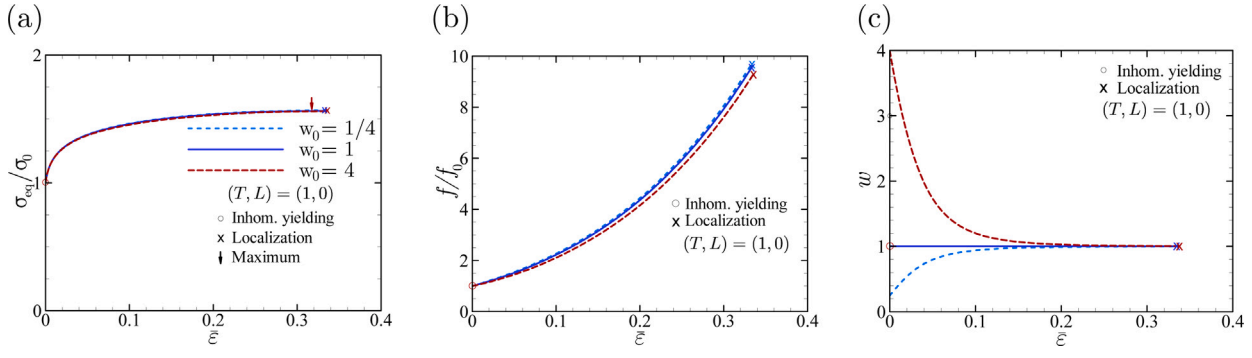

Fig. 16. Overall equivalent stress, Σ_{eq}, normalized by the initial yield stress of the matrix, σ_0 in (43), versus the matrix effective plastic strain, $\bar{\varepsilon}$, for $L = 0$, $T = 1$, $f_0 = 0.001$ and three values of the initial aspect ratio w_0.

In contrast, Fig. 16 provides the overall response and the evolution of f abd w under generalized shear at the same triaxiality $T = 1$. Recall that under inhomogeneous yielding the void aspect ratio evolves faster by virtue of the c term in (41). This may be seen by comparing Fig. 16c with Fig. 15c. Inasmuch as inhomogeneous yielding sets in early (look for the ∘ symbol in Fig. 16a), the initially elongated or flat voids evolve toward a spherical shape long before strain localization occurs. Thus, the initially distinct "microstructures" become indistinguishable beyond a strain of 0.25 or so (see Fig. 16c). This leads to nearly identical evolution of the void volume fraction (Fig. 16b), hence to identical overall responses up to failure (Fig. 16a).

The results in Figs. 15 and 16 provide a justification for the effect of w_0 or its absence in Fig. 12, depending on the stress state. Any other trend can be rationalized in the same way by analyzing the overall response which, itself, is affected by the evolution of state represented by f and w in the isotropic theory. The ensuing Lode dependence results from (i) the Lode dependence of inhomogeneous yielding (primary effect) and (ii) the Lode dependence inherent to strain localization (secondary effect).

6. Discussion

Incorporating inhomogeneous yielding in a constitutive description of porous material plasticity provides a useful framework for analyzing the effects of the third stress invariant on ductile failure, viewed as an instability. Given initial damage descriptors f_0 and w_0, failure loci can be constructed under prescribed loading paths. Under tension-dominated loading, strain localization immediately follows inhomogeneous yielding and the failure criterion essentially reduces to a maximum principal stress criterion with a damage-dependent critical stress. Under combined tension and shear, inhomogeneous yielding prevails from the outset of plastic flow, and since the orientation of the localization band is set by that of the plastic band for inhomogeneous yielding, the failure criterion is bound to depend upon the normal as well as the shear stresses resolved on the band. By way of consequence, a strong J_3 effect emerges on failure loci, *e.g.* under proportional stressing histories as in Fig. 11.

Of particular interest is the general shape of the failure locus in plane stress, Fig. 9. This locus has importance not only for sheet metal fractures but also for tubular specimens under combined tension and torsion. A rationale is needed for the existence of: (i) the cusp at $T = 1/3$ and whether it is inherent; (ii) a ductility minimum in biaxial tension; (iii) a ductility minimum in generalized plane shear ($0 \leq T \leq 1/3$); and for (iv) the relative order of the above two minima; and (v) the infinite ductility in pure shear

($T \to 0$, $L = 0$). All of these features are traceable to the shape of the intrinsic fracture locus, as illustrated through its constant-L sections in Fig. 11 and constant-T sections in Fig. 13.

Biaxial tension corresponds to the $1/3 \le T \le 2/3$ branch in Fig. 9 and a biaxiality ratio $0 \le \rho \le 1$. Over this branch, the Lode parameter spans its full range, from -1 to 1. On the sole basis of a Lode effect, the ductility in equibiaxial tension ($L = +1$) is expected to be higher than uniaxial ductility ($L = -1$); see *e.g.* the $f_0 = 0.001$ locus in Fig. 11. However, the triaxiality is higher in equibiaxial tension and the triaxiality effect here dominates such that the equibiaxial tension ductility emerges as the smaller of the two. Had the triaxiality effect been dominant over the entire biaxial tension regime, the ductility would have been a monotonically decreasing function of T. That a minimum exists in biaxial tension is evidence of a competition between triaxiality and Lode effects in this regime. This explains item (ii) above.

To better understand the cusp, consider generalized plane shear (the $0 \le T \le 1/3$ branch in Fig. 9). Now the biaxiality ratio is negative (in fact the range $-1 \le \rho \le 0$ is sufficient to generate the full branch) but the Lode parameter only varies between -1 and 0; see Eq. (57). As the triaxiality is decreased from $1/3$ one would expect a continuous increase in ductility (see Fig. 13). However, the decrease in T is accompanied with an increase of L from -1 (uniaxial tension or $\rho = 0$) to 0 (pure shear or $\rho = -1$). The decrease in ductility observed in Fig. 9 (just below $T = 1/3$) results from the strongly decreasing trend of $\bar{\epsilon}^{\mathrm{L}}$ in Fig. 11 near $L = -1$. Here, the Lode effect prevails over the triaxiality effect leading to a cusp in the plane stress locus.

Is the cusp inherent to the plane stress fracture locus? Since it results from the competition between the rate of decrease of $\bar{\epsilon}^{\mathrm{L}}$ when L varies from -1 to 0 and the rate of increase of $\bar{\epsilon}^{\mathrm{L}}$ when T decreases from $1/3$ to 0, its very existence depends a priori on the relative magnitudes of those two slopes. Within the confines of the present isotropic theory, it seems that the cusp can hardly be avoided. Even when there is no cusp, the rate of decrease of ductility with decreasing T would undergo an abrupt change in slope at $T = 1/3$. This feature of the model merits further attention as it enables a detailed discussion of conflicting experimental reports, *e.g.* Bao and Wierzbicki (2004) versus Haltom et al. (2013). Following along the same lines, the ductility minimum in generalized plane shear (item (iii)) results from the competition between Lode and triaxiality effects. Just below $T = 1/3$ it is the Lode effect that dominates (hence the cusp) but as the triaxiality is further reduced the effect of T dominates because the Lode effect is not as strong near $L = 0$.

The present isotropic theory predicts unlimited ductility in pure shear. This prediction applies not just to plane stress but more generally to the limit $T \to 0$, irrespective of the value taken by L. This trend is easier to understand when $|L| = 1$. Under such circumstances, homogeneous yielding prevails but the HY criterion does not depend on J_3, and for $T = 0$ the HY constitutive relation predicts zero growth rate of porosity, just like the Gurson model. Thus, strain localization is not predicted. For $L = 0$, inhomogeneous yielding prevails from the outset; yet no localization is predicted. This is because the plastic band is parallel to the plane of maximum shear, and the normal stress, which drives void growth, vanishes on the band.

All of the above features of the plane stress fracture locus, except for the unlimited shear ductility, can be obtained by any *ad hoc* fracture criterion positing, even indirectly, a fracture strain ϵ_{f} as a function of T and L under two conditions: (a) that ϵ_{f} decreases monotonically with increasing T at fixed L; and (b) that ϵ_{f} has the U-shaped, non-monotonic dependence on L of the type shown in Fig. 11. These conditions are met, for example, by the criteria proposed by Bai and Wierzbicki (2010) and Mohr and Marcadet (2015). However, these works proceed from ad hoc stress-based criteria: Mohr–Coulomb and Hosford–Coulomb with little bearing on physical mechanisms. These criteria do predict a finite ductility in pure shear, but that is only because it is posited. Here, we show that an isotropic model is incapable of providing a rationale for failure in shear. In some recent work, Torki and Benzerga (2018) have used an anisotropic version of the multisurface theory whereby inhomogeneous yielding leads to the type of void distortion necessary for failure by direct impingement in simple shear.

That the intrinsic fracture locus exhibits the type of Lode dependence shown in Fig. 11 had previously been evidenced from cell model analyses, *e.g.* Dunand and Mohr (2014) and Vishwakarma and Keralavarma (2019). The challenge is to interpret such trends from first principles. When failure occurs subsequent to strain localization, as inevitably assumed here, it is important to apportion the contribution of the constitutive relation and that of the failure criterion itself to the emergent Lode effect. In particular, it is not necessary for the constitutive law to depend on J_3 for a Lode effect to emerge. Any failure criterion that involves the maximum principle stress, the maximum shear stress or any combination thereof leads to Lode dependence of failure. In particular, the strain localization criterion used here, Eq. (52), would lead to a Lode-dependent strain to failure even with a Lode-independent constitutive relation. For instance, Daehli et al. (2018) have illustrated that, using Gurson's porous material plasticity (see their Fig. 12). The results highlighted in Fig. 11 pave the way for an entirely different picture. It is emphasized that the porous material constitutive relation itself is Lode-dependent (exclusively via inhomogeneous yielding) such that two generic scenarios emerge. Either homogeneous yielding occurs first and it is the Lode-dependent transition to inhomogeneous yielding that causes localization, or inhomogeneous yielding prevails from the outset in which case the entire history of straining prior to failure is Lode-dependent.

Vishwakarma and Keralavarma (2019) had previously illustrated the predictive capabilities of the isotropic multisurface theory in interpreting Lode effects. There are two essential differences between the present results and theirs. First, void shape effects are accounted for here but neglected in previous work. Fig. 12 reveals that void shape has a significant effect for states near generalized tension or compression. On the other hand, Vishwakarma and Keralavarma (2019) obtained nearly indistinguishable loci of inhomogeneous yielding and failure. The difference between their treatment and ours arises from a heuristic amendment to the evolution of strain hardening (compare their Eq. (33) with Eq. (42) here), which was introduced to improve the qualitative and quantitative match with unit cell results. This amendment is certainly important and would deserve more attention.

7. Conclusions

Isotropic constitutive relations for porous material plasticity have been derived from first principles to analyze Lode effects on yield and failure in ductile materials. A key concept not considered in previous analyses is that of inhomogeneous yielding, which corresponds to the finite concentration of plastic deformation in a band, the thickness of which is set by the void size. Under tensile loadings, the transition to inhomogeneous yielding signifies the onset of void coalescence by internal necking, and it eventually represents failure under combined tension and shear. The effect of void shape was incorporated in an average sense with no net texture, a constraint needed to investigate Lode effects with no ambiguity. The key conclusions are as follows.

1. The effective yield surface of a J_2 matrix embedding arbitrarily oriented voids depends on all stress invariants, including J_3. The J_3 dependence manifests strongly at low stress triaxiality and is entirely due to the J_3 dependence of inhomogeneous yielding.
2. Two types of vertices appear in the effective yield surface: those inherent to the surface of inhomogeneous yield and those induced by transition from homogeneous to inhomogeneous yielding.
3. When the multisurface yield criterion is supplemented with simple evolution equations for the internal variables, failure loci can be determined by integrating the constitutive relations along any loading path, and using strain localization as a criterion for failure.
4. In particular, under proportional loadings, the strain to failure is found to be a monotonically decreasing function of the stress triaxiality ratio for all values of the Lode parameter. The strain to failure is predicted to lie on a U-shaped locus when plotted against the Lode parameter, in keeping with cell model analyses.
5. The failure locus in plane stress is shown to possess peculiar features, namely a cusp corresponding to uniaxial loading and two ductility minima in the regimes of biaxial tension and generalized plane shear, the former being the absolute minimum.
6. The infinite ductility predicted under pure (or simple) shear appears to be a direct consequence of the assumption of persistent isotropy. It thus appears that only anisotropic models of porous material plasticity could rationalize a finite shear ductility from first principles.

Declaration of competing interest

The authors declare that they have no known competing financial interests or personal relationships that could have appeared to influence the work reported in this paper.

Acknowledgments

AAB acknowledges financial support from the National Science Foundation (NSF), USA under Grant Number CMMI-1932975. This work is based on the PhD dissertation of MT for which NSF, USA support under Grant Number CMMI-1405226 is gratefully acknowledged.

Appendix A. Surrogate parameters for IY criterion

Consider a statistically isotropic distribution of spheroidal voids with void volume fraction f and aspect ratio $w = a/b$ where a and b are respectively the axial and lateral semi-axes of the void, Fig. A.1a. The distribution of the location, size and orientation of the voids is assumed to be random.[1] Recall that the orientation of an individual void is determined by unit vector $\mathbf{v}$, Fig. A.1c.

The models invoked for inhomogeneous yielding (Torki et al., 2015; Keralavarma and Chockalingam, 2016) are applicable to a transversely isotropic periodic array of cylindrical voids of equal volume as depicted in Fig. A.1b. In this case, the plastic (localization) band normal $\mathbf{n}$ is identified with $\mathbf{v}$ and criteria (16) or (18) may be used as is. For a random distribution (Fig. A.1a) the orientation of the plastic band is determined solely by the macroscopic stress state, *i.e.* $\mathbf{n} = \mathbf{n}(\boldsymbol{\Sigma})$; see Eq. (31). Thus, in order to average allowable stresses over all possible void orientations $\mathbf{v}$, an effective band porosity and an effective void aspect ratio must be defined. These effective quantities are called surrogate parameters. For a statistically isotropic distribution of voids, the cell aspect ratio is unity and

$$f = \frac{\bar{R}^2 \bar{h}}{L^3} \tag{A.1}$$

The following scheme is used to determine the aspect ratio of the surrogate cylindrical void, $\bar{w}$, depicted in Fig. A.1d.

First, an individual spheroidal void embedded in a concentric spherical shell is considered as shown in Fig. A.1(c), where the void axis, $\mathbf{v}$, is oriented at some angle θ with respect to $\mathbf{n}$. The radius of the spherical shell, L, is chosen such that the volume fraction of the void satisfies $ab^2/L^3 = f$. The area of the trace of the void on a section plane with normal $\mathbf{n}$ is calculated and equated with the cross-sectional area of a surrogate cylindrical void of radius $R(\theta)$ directed along $\mathbf{n}$. Let $\chi(\theta) = R(\theta)/L$ denote the ligament parameter

[1] For finite porosity, the distribution of locations cannot be uniformly random as in a Poisson process. Some degree of clustering would occur because of excluded volume arguments (Benzerga, 2000). This detail does not matter for homogeneous yield models where porosity is dilute but should be assessed further for inhomogeneous yielding. Typical HY to IY transitions occur for $f \sim 0.01$ which may be treated as dilute within limits.

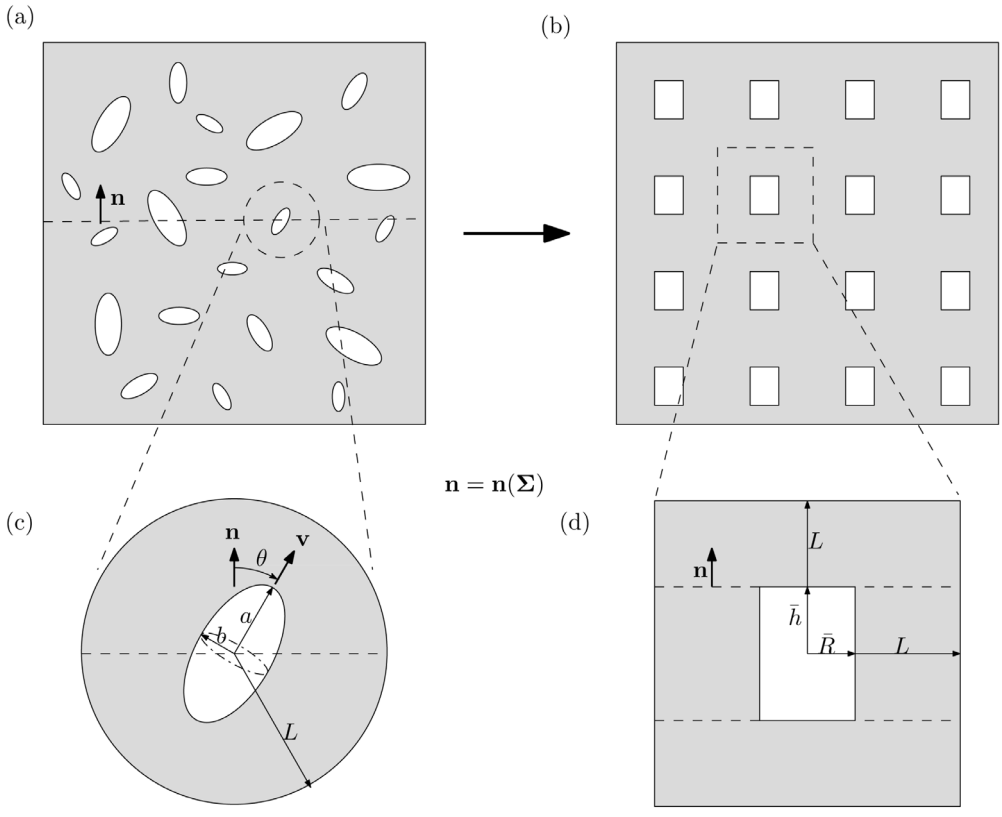

Fig. A.1. (a) Random distribution of spheroidal voids. (b) Corresponding surrogate microstructure. (c) Elementary cell in (a). (d) Elementary cell in (b).

of the surrogate void such that its square χ^2 equals the porosity within the plastic band, identified by the ratio of the area of the trace of the void to that of the surrogate cell on the plane with normal **n**. The resulting expression is

$$\chi^2 = \frac{\left(\sqrt{w}f\right)^{2/3}}{\sqrt{1+(w^2-1)\cos^2\theta}} \tag{A.2}$$

Next, the average porosity in the band, f_b, *i.e.* the void volume fraction inside a band of width equal to the height of the void in Fig. A.1d, is determined as the orientation average of χ^2. This leads to the relation

$$f_b = \frac{\bar{R}^2}{L^2} = \langle\chi^2\rangle_\theta = \frac{2}{\pi}\int_0^{\frac{\pi}{2}} \chi^2 \, \mathrm{d}\theta \tag{A.3}$$

The above expression results in an elliptic integral, so that the solution for f_b can be written in the form

$$f_b = \begin{cases} \left(\frac{f}{w}\right)^{2/3} \frac{2}{\pi} K\left(1-\frac{1}{w^2}\right) & (w \geq 1) \\ \left(\sqrt{w}f\right)^{2/3} \frac{2}{\pi} K\left(1-w^2\right) & (w < 1) \end{cases} \tag{A.4}$$

where K denotes the complete elliptic integral of the first kind. The argument of K in the above expressions is the square of void eccentricity, which reads as $1-1/w^2$ and $1-w^2$ for $w \geq 1$ and $w \leq 1$, respectively. Given the value of f_b, the aspect ratio of the surrogate void $\bar{w} = \bar{h}/\bar{R}$ can be evaluated using the geometric relationship $\bar{w} = f/f_b^{3/2}$ based on (A.1). This gives the desired expression (22).

Fig. A.2 shows the variation of so-determined $\bar{w}$ as a function of w. Notice that $\bar{w}$ varies in an approximately linear fashion with w except for very small values of w, *i.e.* highly oblate voids. Also, the slope of the quasi-linear part is much smaller than unity, indicating that the effect of the void shape is quite small when the voids are oriented randomly. A reasonable approximation that avoids the special function in Eq. (22) is to use a linear fit for the above curve passing through the $w = 1$ point, of the form

$$\bar{w} = k(w-1)+1 \tag{A.5}$$

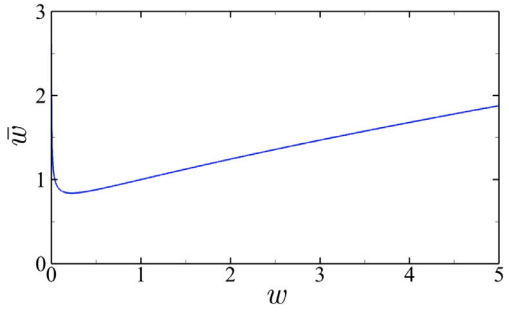

Fig. A.2. Surrogate versus actual void aspect ratio.

where the value of k falls in the approximate range of $0.2 < k < 0.25$. This approximation proves reasonable for all but highly oblate voids. It has been used in the results shown in the main text.

Appendix B. Macroscopic IY criterion by ensemble averaging

For arbitrary void and band orientations, respectively $\mathbf{v}$ and $\mathbf{n}$, the unknown mesoscale criterion would take the form: $\mathcal{F}^{\mathrm{I}}(\boldsymbol{\sigma}; f_{\mathrm{b}}, w, \mathbf{v}, \mathbf{n})$. Criteria (16) and (18) correspond to the special case $\mathbf{v} = \mathbf{n}$. To obtain an isotropic criterion, one needs to carry out ensemble averaging over the two random variables $\mathbf{v}$ and $\mathbf{n}$. The result should not depend on the order in which the two variables are considered. In practice, a technical difficulty arises because a meso-scale yield model that accounts for arbitrary void and cell orientations is lacking. If one assumes that the true criterion depends on the orientation of the void relative to that of the band, then a reasoning similar to that of Appendix A may be developed for arbitrarily oriented voids within a *fixed* band with orientation $\mathbf{n}$ prior to carrying out an extremization as in (23).

Under such circumstances, an effective yield function per band is written which takes the form in, say (16) but with $\mathcal{S}$, $\mathcal{V}$, etc. replaced with $\bar{\mathcal{S}} = \mathcal{S}(f_{\mathrm{b}}, \bar{w})$ and $\bar{\mathcal{V}} = \mathcal{V}(f_{\mathrm{b}})$ where f_{b} and $\bar{w}$ are defined relative to the band. Using the properties of the Heaviside function, it is straightforward to verify the following inequality

$$|\Sigma_{\mathrm{n}}| - \bar{\mathcal{S}} \le \langle|\sigma_{\mathrm{n}}|\rangle - \bar{\mathcal{S}} \le |\sigma_{\mathrm{n}}| - \bar{\mathcal{S}} \;\therefore\; \mathcal{H}(|\Sigma_{\mathrm{n}}| - \bar{\mathcal{S}}) \le \mathcal{H}(|\sigma_{\mathrm{n}}| - \bar{\mathcal{S}}) \tag{B.1}$$

Hence, one can write

$$\left(\frac{|\sigma_{\mathrm{n}}| - \bar{\mathcal{S}}}{\bar{\mathcal{V}}}\right)\mathcal{H}(|\Sigma_{\mathrm{n}}| - \bar{\mathcal{S}}) \le \sqrt{1 - \left(\frac{\tau_{\mathrm{n}}}{\bar{\mathcal{T}}}\right)^2} \tag{B.2}$$

Averaging both sides of the above inequality over all meso-scale domains contained in the localization band, we obtain

$$\left(\frac{\langle|\sigma_{\mathrm{n}}|\rangle - \bar{\mathcal{S}}}{\bar{\mathcal{V}}}\right)\mathcal{H}(|\Sigma_{\mathrm{n}}| - \bar{\mathcal{S}}) \le \left\langle\sqrt{1 - \left(\frac{\tau_{\mathrm{n}}}{\bar{\mathcal{T}}}\right)^2}\right\rangle \tag{B.3}$$

Since $\sqrt{1-x^2}$ is a concave function of x, we have $\langle\sqrt{1-x^2}\rangle \le \sqrt{1-\langle x\rangle^2}$. Also, we have $\langle|x|\rangle \ge |\langle x\rangle|$. Using the above two results in (B.3), we get

$$\left(\frac{|\langle\sigma_{\mathrm{n}}\rangle| - \bar{\mathcal{S}}}{\bar{\mathcal{V}}}\right)\mathcal{H}(|\Sigma_{\mathrm{n}}| - \bar{\mathcal{S}}) \le \sqrt{1 - \left(\frac{\langle\tau_{\mathrm{n}}\rangle}{\bar{\mathcal{T}}}\right)^2} \tag{B.4}$$

Using the definition of $\boldsymbol{\Sigma}$, one can further show that $\langle\sigma_{\mathrm{n}}\rangle = \Sigma_{\mathrm{n}}$ while $\langle\tau_{\mathrm{n}}\rangle \ge \Sigma_{\mathrm{sh}}$. Substituting in (B.4) yields

$$\left(\frac{|\Sigma_{\mathrm{n}}| - \bar{\mathcal{S}}}{\bar{\mathcal{V}}}\right)\mathcal{H}(|\Sigma_{\mathrm{n}}| - \bar{\mathcal{S}}) \le \sqrt{1 - \left(\frac{\Sigma_{\mathrm{sh}}}{\bar{\mathcal{T}}}\right)^2} \tag{B.5}$$

The macroscopic yield criterion for inhomogeneous plasticity in an arbitrarily oriented localization band of voids is obtained by rearranging (B.5) to write

$$\bar{\mathcal{F}}^{\mathrm{I}}(\boldsymbol{\Sigma}; f_{\mathrm{b}}, \bar{w}, \mathbf{n}) = \left(\frac{|\Sigma_{\mathrm{n}}| - \bar{\mathcal{S}}}{\bar{\mathcal{V}}}\right)^2 \mathcal{H}(|\Sigma_{\mathrm{n}}| - \bar{\mathcal{S}}) + \left(\frac{\Sigma_{\mathrm{sh}}}{\bar{\mathcal{T}}}\right)^2 - 1 \le 0 \tag{B.6}$$

If this intermediate step is used in (23) the final outcome will be exactly the same as criterion (34) by virtue of the heuristics underlying the surrogate parameters. This justifies the "shortcut" employed in the main text for brevity.

Note that if the modified Torki–Benzerga–Leblond model is used, then

$$\bar{\mathcal{F}}^{\mathrm{I}}(\boldsymbol{\Sigma}; f_{\mathrm{b}}, \bar{w}, \mathbf{n}) = \left(\frac{|\Sigma_{\mathrm{n}}| - t(f_{\mathrm{b}}, \bar{w})\bar{\mathcal{S}}}{b\bar{\mathcal{V}}}\right)^2 \mathcal{H}(|\Sigma_{\mathrm{n}}| - \bar{\mathcal{S}}) + \left(\frac{\Sigma_{\mathrm{sh}}}{l(f_{\mathrm{b}}, \bar{w})\bar{\mathcal{T}}}\right)^2 - 1 \le 0 \tag{B.7}$$

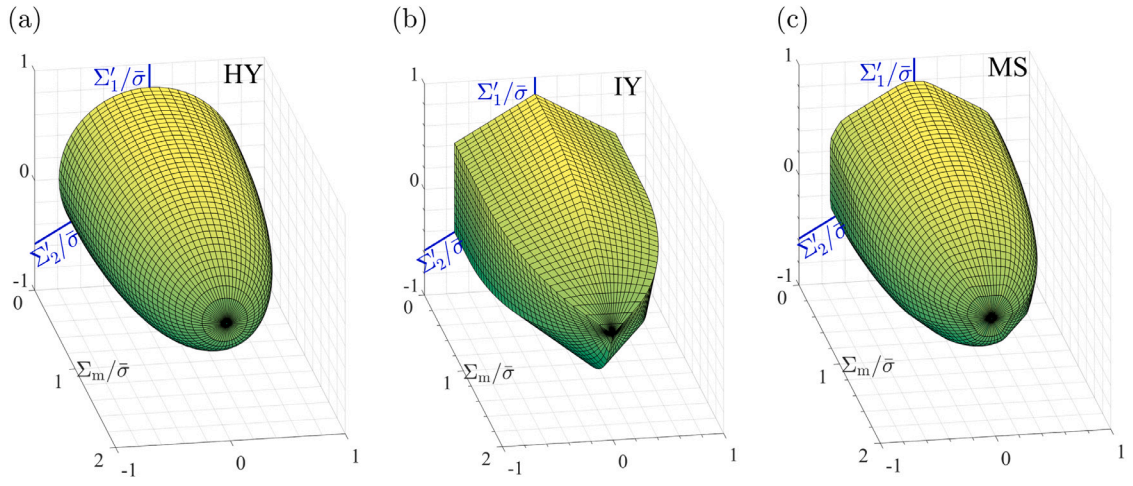

Fig. A.3. Yield surfaces of a porous material with void volume fraction $f = 0.03$ and aspect ratio $w = 1/5$: (a) homogeneous yielding, (b) inhomogeneous yielding, and (c) effective surface shown in Fig. 2c.

where t, b and l are heuristic parameters introduced in Torki et al. (2017). Calibration using the finite elements limit loads of Keralavarma (2017) leads to $b = 0.95$, $t = (t_0 + t_1\sqrt{f_b})\bar{w}/(1 + (t_0 + t_1\sqrt{f_b})\bar{w})$ with $t_0 = -0.84$, $t_1 = 12.9$, and $l = 1$.

Appendix C. Alternative macroscopic iy criterion

If IY criterion (18) is used at the mesoscale instead of (16) then the criterion for internal necking is:

$$\mathcal{F}^{\mathrm{In}}(\Sigma_i) = |\Sigma_i| - \frac{\bar{\sigma}}{\beta}\ln\frac{1}{f_b} \tag{C.1}$$

where β is defined in $(19)_1$, and the criterion for combined tension and shear is determined by satisfying (18), with σ_n and τ_n being replaced with their macroscopic counterparts Σ_n and Σ_{sh}, respectively, using the Reuss approximation. In addition, the expression for $\tilde{\Sigma}$ in Eq. (25) reads:

$$\tilde{\Sigma}(\boldsymbol{\Sigma}, \mathbf{n}^*) = 2\left[\Sigma_n - \frac{1}{3}\beta\bar{\sigma}f_b \sinh\left(\beta\frac{\Sigma_n}{\bar{\sigma}}\right)\right] \tag{C.2}$$

The solution of Eq. (25) using (C.2) yields the normal stress Σ_n and the orientation of the IY plane through $(31)_2$. The corresponding shear stress is obtained from the Mohr identity, Eq. (30).

Elimination of the hyperbolic functions between (18) and (25) and the normal stress using (30), leads to a biquadratic equation for the shear stress Σ_{sh}

$$\Sigma_{sh}^4 - 2S_1\bar{\sigma}^2\Sigma_{sh}^2 + S_2\bar{\sigma}^4 = 0 \tag{C.3}$$

where

$$S_1 = \frac{1}{3}(1 + f_b^2) - \frac{2}{\beta^2} \quad , \quad S_2 = \frac{1}{9}(1 - f_b^2)^2 - \left(\frac{\Sigma_1 - \Sigma_2}{\beta\bar{\sigma}}\right)^2$$

A valid solution for Σ_{sh} must fall in the range $0 < \Sigma_{sh} < |\Sigma_1 - \Sigma_2|/2$ for IY to occur under combined tension and shear on a plane parallel to the $\mathbf{e}_3$ principal axis; see Appendix A in Keralavarma (2017) for details. The corresponding IY plane orientation is then obtained from Eq. $(31)_1$.

Unfortunately, elimination of Σ_n and Σ_{sh} from yield criterion (18) using the solution of the above set of equations proves difficult. Hence, an exact closed form counterpart of the yield function under combined tension and shear $\mathcal{F}^{\mathrm{I}}_{\mathrm{sh}}(\Sigma_1, \Sigma_2)$, defined in (33) for criterion (16), cannot be obtained analytically. However, approximate, yet accurate, closed form expression for $\mathcal{F}^{\mathrm{I}}_{\mathrm{sh}}(\Sigma_1, \Sigma_2)$ using the KC model has been derived (see Reddi et al., 2019, Eq. 16), which can be used in place of the exact solution.

Two more similar yield functions for IY to occur on planes parallel to the $\mathbf{e}_1$ and $\mathbf{e}_2$ axes can be obtained by cyclic permutation of the indices 1,2 and 3 in the above analysis. The final *isotropic* criterion for IY is then obtained by combining the six different criteria derived above using (34). The counterparts to Eqs. (26) and (33) are so obtained.

The normal to the yield surface that appears in the macroscopic flow rule (37) now reads

$$\mathbf{N} = \frac{3}{\bar{\sigma}^2}\mathbf{m}\cdot(\boldsymbol{\Sigma}\mathbf{n})(\mathbf{m}\otimes\mathbf{n} + \mathbf{n}\otimes\mathbf{m}) + 2f_b\frac{\beta}{\bar{\sigma}}\sinh\left(\beta\frac{\Sigma_n}{\bar{\sigma}}\right)\mathbf{n}\otimes\mathbf{n} \tag{C.4}$$

where $\mathbf{m} = (\boldsymbol{\Sigma}\mathbf{n} - \Sigma_n\mathbf{n})/|\boldsymbol{\Sigma}\mathbf{n} - \Sigma_n\mathbf{n}|$ is the unit vector along the resolved shear traction on the IY plane.

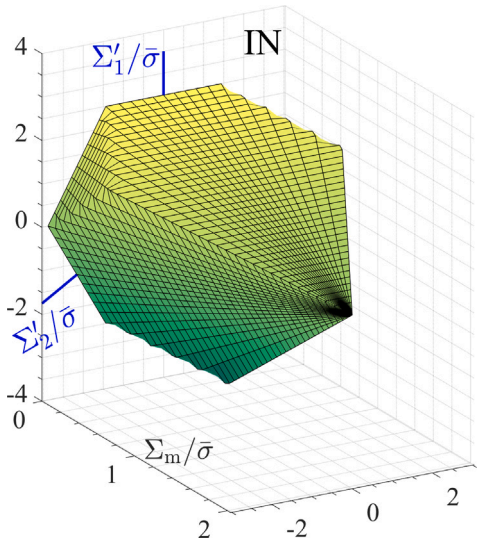

Fig. A.4. Internal necking yield locus for $f = 0.03$ and $w = 1$.

Appendix D. Examples of 3D yield surfaces

Illustrations of yield surfaces described by the multisurface criterion, Eq. (36), were provided in Fig. 2. Fig. A.3 provides details regarding the two surfaces described by $\bar{F}^{\mathrm{H}}(\boldsymbol{\Sigma}; f, w) = 0$ for homogeneous yielding (HY) and $\bar{F}^{\mathrm{I}}(\boldsymbol{\Sigma}; f_{\mathrm{b}}, \bar{w}) = 0$ for inhomogeneous yielding (IY) with the multisurface (MS) being an envelope of the two. Fig. A.3 illustrates this for $w = 1/5$ for which intersections between the two surfaces are most consequential. In particular, the vertex on the hydrostatic axis disappears from the effective surface, Fig. A.3c, because HY is predicted to be active under pure hydrostatic loading in that case.

It may also be useful to the reader to depict the surface corresponding to internal necking alone, viewed as an isotropic yield criterion, Fig. A.4. The surface shown corresponds to Eq. (26) for $f = 0.03$ and $w = 1$.

The internal necking surface alone exhibits pressure and Lode-dependence. This is so because it reduces to a (conditional) maximum principal stress criterion. At low amounts of mean normal stress, say on the π-plane, octahedral sections are hexagons. Whether the major stress is axial ($\theta = 0$) or lateral ($\theta = \pi/3$) internal necking is predicted. The latter is not the exact prediction, since in that case coalescence in columns is known to prevail (Gologanu et al., 2001), but is not accounted for here. However, at sufficiently high triaxiality octahedral sections become triangular. This means that only internal necking perpendicular to a principal stress direction is possible, with the evident indeterminacy of the plane of necking when all normal stresses are equal (vertex).

References

Bai, Y., Wierzbicki, T., 2010. Application of extended Mohr–Coulomb criterion to ductile fracture. Int. J. Fract. 161, 1–20.
Bao, Y., Wierzbicki, T., 2004. On fracture locus in the equivalent strain and stress triaxiality space. Int. J. Mech. Sci. 46, 81–98.
Barsoum, I., Faleskog, J., 2007. Rupture mechanisms in combined tension and shear—-Experiments. Int. J. Solids Struct. 44, 1768–1786.
Benzerga, A.A., 2000. Rupture Ductile des Tôles Anisotropes (Ph.D. thesis). Ecole Nationale Supérieure des Mines de Paris.
Benzerga, A.A., 2002. Micromechanics of coalescence in ductile fracture. J. Mech. Phys. Solids 50, 1331–1362.
Benzerga, A.A., Leblond, J.-B., 2010. Ductile fracture by void growth to coalescence. Adv. Appl. Mech. 44, 169–305.
Benzerga, A.A., Leblond, J.-B., 2014. Effective yield criterion accounting for microvoid coalescence. J. Appl. Mech. 81, 031009.
Clausing, D.P., 1970. Effect of plastic state on ductility and toughness. Int. J. Fract. Mech. 6, 71–85.
Daehli, L.E., Morin, D., Borvik, T., Hopperstad, O.S., 2018. A Lode-dependent Gurson model motivated by unit cell analyses. Eng. Fract. Mech. 190, 299–318.
Dunand, M., Mohr, D., 2011. On the predictive capabilities of the shear modified Gurson and the modified Mohr–Coulomb fracture models over a wide range of stress triaxialities and Lode Angles. J. Mech. Phys. Solids 59, 1374–1394.
Dunand, M., Mohr, D., 2014. Effect of Lode parameter on plastic flow localization after proportional loading at low stress triaxialities. J. Mech. Phys. Solids 66, 133–153.
Gologanu, M., Leblond, J.-B., Devaux, J., 1993. Approximate models for ductile metals containing non-spherical voids – case of axisymmetric prolate ellipsoidal cavities. J. Mech. Phys. Solids 41 (11), 1723–1754.
Gologanu, M., Leblond, J.-B., Perrin, G., Devaux, J., 1997. Recent extensions of Gurson's model for porous ductile metals. In: Suquet, P. (Ed.), Continuum Micromechanics. In: CISM Lectures Series, Springer, New York, pp. 61–130.
Gologanu, M., Leblond, J.-B., Perrin, G., Devaux, J., 2001. Theoretical models for void coalescence in porous ductile solids – II: Coalescence in columns. Int. J. Solids Struct. 38, 5595–5604.
Gurson, A.L., 1977. Continuum theory of ductile rupture by void nucleation and growth: Part I– Yield criteria and flow rules for porous ductile media. J. Eng. Mater. Technol. 99, 2–15.
Hadamard, J., 1903. Leçons sur la Propagation des Ondes et les Équations de l'Hydrodynamique. Librairie Scientifique, A. Herrmann, Paris, chapter 6.
Haltom, S.S., Kyriakides, S., Ravi-Chandar, K., 2013. Ductile failure under combined shear and tension. Int. J. Solids Struct. 50, 1507–1522.
Hill, R., 1950. The Mathematical Theory of Plasticity. Clarendon Press, Oxford.

Johnson, G.R., Hoegfeldt, J.M., Lindholm, U.S., Nagy, A., 1983. Response of various metals to large torsional strains over a large range of strain rates – Part 1: Ductile metals. J. Eng. Mater. Technol. 105, 42–47.
Keralavarma, S.M., 2017. A multi-surface plasticity model for ductile fracture simulations. J. Mech. Phys. Solids 103, 100–120.
Keralavarma, S.M., Benzerga, A.A., 2010. A constitutive model for plastically anisotropic solids with non-spherical voids. J. Mech. Phys. Solids 58, 874–901.
Keralavarma, S.M., Chockalingam, S., 2016. A criterion for void coalescence in anisotropic ductile materials. Int. J. Plast. 82, 159–176.
Keralavarma, S.M., Reddi, D., Benzerga, A.A., 2020. Ductile failure as a constitutive instability in porous plastic solids. J. Mech. Phys. Solids 139, 103917.
Koplik, J., Needleman, A., 1988. Void growth and coalescence in porous plastic solids. Int. J. Solids Struct. 24, 835–853.
Madou, K., Leblond, J.-B., 2012. A Gurson-type criterion for porous ductile solids containing arbitrary ellipsoidal voids – II: Determination of yield criterion parameters. J. Mech. Phys. Solids 60, 1037–1058.
Mohr, D., Marcadet, S.J., 2015. Micromechanically-motivated phenomenological hosford-coulomb model for predicting ductile fracture initiation at low stress triaxialities. Int. J. Solids Struct. 67–68, 40–55.
Morin, L., Leblond, J.-B., Benzerga, A.A., 2015. Coalescence of voids by internal necking: theoretical estimates and numerical results. J. Mech. Phys. Solids 75, 140–158.
Morin, L., Leblond, J.-B., Benzerga, A.A., Kondo, D., 2016. A unified criterion for the growth and coalescence of microvoids. J. Mech. Phys. Solids 97, 19–36.
Nahshon, K., Hutchinson, J.W., 2008. Modification of the Gurson model for shear failure. Eur. J. Mech. 27, 1–17.
Pineau, A., Benzerga, A.A., Pardoen, T., 2016. Failure of metals I. Brittle and Ductile fracture. Acta Mater. 107, 424–483.
Reddi, D., Areej, V.K., Keralavarma, S.M., 2019. Ductile failure simulations using a multi-surface coupled damage-plasticity model. Int. J. Plast. 118, 190–214.
Rice, J.R., 1976. The localization of plastic deformation. In: Koiter, W.T. (Ed.), 14th Int. Cong. Theoretical and Applied Mechanics. North–Holland, Amsterdam, pp. 207–220.
Rice, J.R., Tracey, D.M., 1969. On the enlargement of voids in triaxial stress fields. J. Mech. Phys. Solids 17, 201–217.
Roth, C.C., Morgeneyer, T.F., Cheng, Y., Helfen, L., Mohr, D., 2018. Ductile damage mechanism under shear-dominated loading: In-situ tomography experiments on dual phase steel and localization analysis. Int. J. Plast. 109, 169–192.
Scales, M., Tardif, N., Kyriakides, S., 2016. Ductile failure of aluminum alloy tubes under combined torsion and tension. Int. J. Solids Struct. 97–98, 116–128.
Torki, M.E., 2019. A unified criterion for void growth and coalescence under combined tension and shear. Int. J. Plast. 119, 57–84.
Torki, M.E., Benzerga, A.A., 2018. Micromechanics-based constitutive relations for post-localization analysis. MethodsX 5, 1431–1439.
Torki, M.E., Benzerga, A.A., Leblond, J.-B., 2015. On void coalescence under combined tension and shear. J. Appl. Mech. 82 (7), 071005.
Torki, M.E., Tekoglu, C., Leblond, J.-B., Benzerga, A.A., 2017. Theoretical and numerical analysis of void coalescence in porous ductile solids under arbitrary loadings. Int. J. Plast. 91, 160–181.
Tvergaard, V., 1982. On localization in ductile materials containing spherical voids. Int. J. Fract. 18, 237–252.
Vishwakarma, V., Keralavarma, S.M., 2019. Micromechanical modeling and simulation of the loading path dependence of ductile failure by void growth to coalescence. Int. J. Solids Struct. 166, 135–153.